A novel bio-inspired microstructure for improved compressive performance of multidirectional CFRP laminates

Torquato Garulli [*,1], Tomas J. Katafiasz, Emile S. Greenhalgh, Silvestre T. Pinho

Department of Aeronautics, Imperial College London, South Kensington Campus, SW7 2AZ London, United Kingdom

ABSTRACT

In this work, we design, manufacture, test and discuss the first bio-inspired microstructural concept to enhance longitudinal compressive performance of multidirectional (MD) Carbon Fibre Reinforced Polymer (CFRP) laminates. To do so, we take inspiration from biologically occurring layered materials; one remarkable example being the anchoring spicula of the deep-sea glass sponge *Monoraphis chuni*. We designed numerically various concepts and then devised a strategy to reproduce, in a MD CFRP laminate, the characteristic alternation of stiff and soft regions observed in this material, followed by a bespoke procedure to manufacture the laminate. We evaluated their performances by means of small-scale notched compression tests and direct comparison with an industrially relevant baseline laminate. Our results show that the proposed concept led to a statistically significant increase in the failure load and in the average ligament specific stress at failure. Furthermore, the designed microstructure showed potential to delay damage initiation from a stress concentration and to arrest damage propagation. We conclude that the presented microstructural concept is potentially of great value for the design of lightweight structures undergoing compression loading.

1. Introduction

In recent years, the use of high performance CFRPs in structural applications has been steadily growing. Due to their excellent properties, these materials allow to design highly efficient structures, thus being extremely valuable in sectors like aviation and transportation in general. While their adoption has already had a positive environmental impact [1], further results could be achieved by addressing still-standing weaknesses of these materials. Among such weaknesses, performance under longitudinal compression is one of the most important, as it remains one limiting factor in many applications. Typically, the longitudinal compressive strength of unidirectional (UD) CFRPs is considerably lower than their tensile strength [2,3]. This is because compressive failure most often stems from a material instability process: in the matrix regions between initially misaligned fibres, significant shear stress develops, which promotes further fibre rotation; with increasing load, shear stress in the matrix reaches values high enough to cause large plastic strain, matrix shear failure or interphase failure; this eventually leads to unstable fibre rotation, kinkband formation and final collapse [4–7]. In MD laminates, the failure process is even more complex, and it encompasses subcritical damage in off-axis plies as

well as delamination [8–12]. Due to this complexity, devising effective strategies to improve performance of MD CFRP laminates under compression is a challenging task.

In this context, biological materials can be a valuable source of inspiration to devise novel microstructural solutions [13,14]. Bio-inspired designs have shown great potential and have been developed for improved damage tolerance [13,15–18], energy absorption [19–21], ballistic protection [22], containment [23,24] and other applications [25–31]. Among the most inspirational solutions observed in nature, one is represented by layered microstructures, showing a periodic alternation of stiff (and usually strong) and soft (and usually weak) layers, that possess excellent properties in terms of strength and fracture toughness [32,33]. One notable example of this is the giant anchoring spicula of the deep-sea sponge *Monorhaphis chuni* [34], reported to be the largest biosilica structure on earth [35], Fig. 1 [36]. Relevantly, *Monorhaphis chuni* exploits this microstructural design to deal with both compressive and tensile stress states, generated by the bending of its spicula under the action of ocean currents [36]. A number of studies elucidated the prominent role played by soft layers: they promote crack deflection [33,36], can blunt a propagating crack, thus mitigating stress
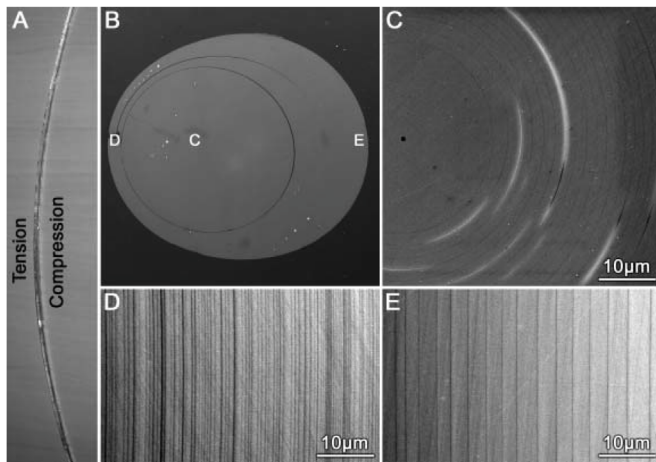

Fig. 1. Global view of the giant anchoring spicula of *Monoraphis chuni* (A), transversal cross-section (B), and high-magnification details of the microstructure at different locations (as indicated in B): central cylindrical core (C), tensile side (D) and compressive side (E). Reproduced from [36] with permission from John Wiley and Sons.

Fig. 2. Schematic representation of the microstructural design strategy proposed.

intensity at its tip [33] and they create a periodical alternation of stiffness and/or strength properties that gives rise to the so called *inhomogeneity effect* [37–39], often capable of completely arresting a propagating crack. This has recently inspired a series of studies presenting synthetic designs inspired by layered biological materials [40–44]. To date, however, no bio-inspired design has been proposed to improve longitudinal compressive performance of CFRP laminates.

In view of this, the goal of this work is to present, for the first time in the literature, a bio-inspired microstructural solution specifically tailored to MD CFRP laminates undergoing longitudinal compression. We take inspiration from natural layered materials to try and replicate the inhomogeneity effect and the crack blunting mechanisms typically observed in nature. We started by designing the microstructure and proceeded manufacture it, for which we developed a bespoke multi-step manufacturing procedure. We then assessed its performance against an industrially-relevant laminate by means of small-scale notched compression tests. We used several different experimental techniques to gain insight on the behaviour of the newly designed microstructure and performed Finite Element (FE) analyses to enrich our understanding of the specimens behaviour.

The paper is structured as follows: Section 2 presents the design of the new microstructure, firstly from a conceptual point of view and then in relation to the specific configuration used in this study; Section 3 provides detailed information about the manufacture process and the test techniques we used in this study; Section 4 describes the FE models we created; Section 5 presents the results of our tests, which are then discussed in Section 6; conclusions are presented in Section 7. An Appendix is included Appendix A to provide additional details relevant to our material selection process.

2. Microstructure design

2.1. Conceptual approach

While the approach presented can be easily generalised, we focus here, for simplicity, on traditional *quad* MD CFRP laminates, i.e. all those laminates that use 0°, ±45° and 90° oriented plies. The original solution we propose in this study is to reproduce the periodic alternation between stiff (and/or strong) and soft (and/or weak) materials observed in biological layered materials in the load bearing 0° plies of the laminate. We aim to achieve this by introduction in these plies of a soft (and/or weak) phase (i.e. whose Young's modulus and strength
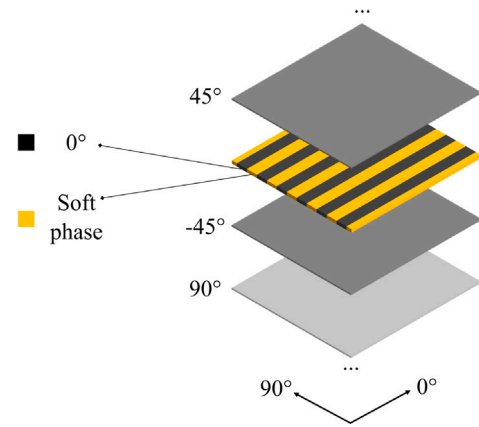
are about one order of magnitude, at least, smaller than those of the CFRP material considered), in the form of continuous strips aligned with the load direction, as shown in the schematic sketch in Fig. 2. The choice not to introduce a soft phase in other layers reflects, and exploits, the facts that layers with different orientations will contribute differently to the global elastic properties of the laminate and will behave differently during the compressive failure process, as will be clarified below. It is also worth mentioning that the design choices made here are purposely targeting the case of in-plane compression loading, while different microstructural solutions may be best suited for different load cases. The rationale behind our strategy is explained in detail in the following.

Exploiting the inhomogeneity effect. The inhomogeneity effect is one major factor determining the exceptional properties of biological layered materials. It consists in a change in crack driving force during propagation trough a microstructure with changing stiffness and/or strength, with the most beneficial form being a combined stiffness and strength inhomogeneity [44]. Specifically, a rise in crack driving force occurs when the crack approaches a stiff-to-soft (or strong-to-weak) transition and a drop occurs when it approaches a soft-to-stiff (or weak-to-strong) one [37]. In many cases, such drop is sufficient to arrest crack propagation, imposing re-nucleation at the next stiff region, which greatly improves overall fracture properties.

When considering MD CFRP laminates under longitudinal compression, mechanical properties are mostly determined by 0° plies, with very little to negligible contribute from off-axis (±45° and 90°) plies. Hence, the proposed microstructural modification allows to obtain a desirable in-plane alternation of stiff/strong and soft/weak regions by creating in the laminate longitudinal strip-shaped regions where no 0° CFRP material exists (thus with very low longitudinal stiffness and strength), alternated with regions where 0° CFRP material exists (hence much stiffer and stronger). This way, the inhomogeneity effect can be exploited.

Preserving other laminate properties. While an in-plane alternation of stiff/strong and soft/weak regions in terms of longitudinal properties is desired, it is important that the devised microstructure does not impair other properties of the laminate, such as its transverse modulus and in-plane shear modulus. These properties are mostly determined by off-axis plies (most often 90° and ±45° plies), with a contribution from 0° plies that is small or even negligible. Consequently, the proposed selective modification of the 0° plies, which fully preserves the integrity of off-axis plies, is expected to have a minor effect on these properties, as desired.

Blunting a kinkband. Damage initiation and propagation in a MD laminate under in-plane compression involves multiple different mechanisms, but final collapse of the laminate is dictated by failure of 0° plies, and the subsequent loss of load bearing capability. This usually
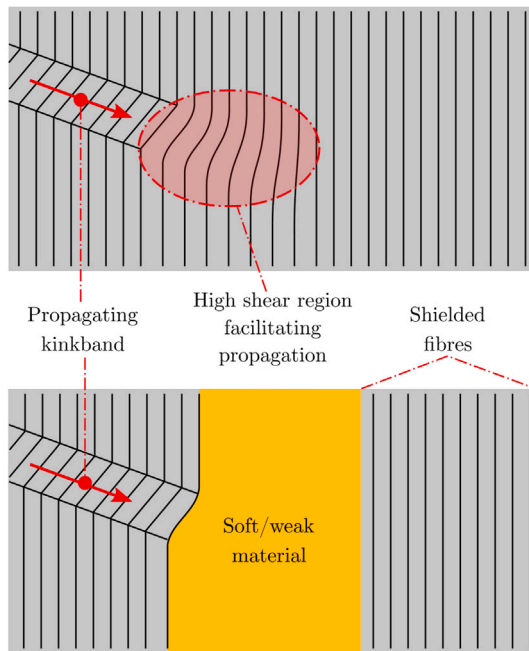
Fig. 3. Schematic representation of the beneficial effect of a region of soft/weak material on kinkband propagation. During formation and propagation of a kinkband, a region of high shear stress and fibre deformation forms ahead of the kinkband [47], which facilitates further propagation. The presence of a soft/weak material allows for local deformation to occur without significant shear stress being transferred to the next region of load bearing fibres.

happens by kinkband formation and propagation, possibly facilitated by delamination at neighbouring ply interfaces, while off-axis plies only suffer sub-critical damage prior to failure. Furthermore, both delamination and off-axis plies damage can be heavily mitigated by the use of thin-ply composites, thus making compressive failure of a MD laminate even more dominated by the failure of 0° plies [45]. Since kinkband propagation in 0° plies presents some similarities to tensile crack propagation [46], the presence of soft/weak material regions (known to enhance fracture properties by significantly blunting a propagating crack, due to their reduced elastic modulus and to localised inelastic deformation [33]) may be beneficial to blunt kinkband propagation too. This seems even more sensible when considering that kinkband propagation is not only driven by remote loading, but also by local conditions: fibre kinking leads to increased shear deformation and shear stresses ahead of the tip of the kinkband itself, that in turn then facilitate further kinking failure in this region, and thus kinkband propagation, see Fig. 3; this positive feedback mechanism may be interrupted by the presence of a soft/weak phase that physically separates 0° load bearing strips of material and that is unable to transfer significant shear stress due to its reduced mechanical properties.

2.2. Configuration design

Due to the advantages mentioned in Section 2.1, we selected for this study a thin-ply carbon/epoxy composite system, namely MR70/TP402, commercially available from North Thin Ply Technology (NTPT), with a Fibre Areal Weight (FAW) of 15 gsm. Its constituents properties are reported in Table 1, while ply properties are reported in Table 2. To create soft inclusions, we used a polymethacrylimide (PMI) foam material, namely Rohacell© RC200SL, kindly provided by Yoneshima Felt Ltd. in the form of ultra-thin (70 μm thick) sliced sheets. Properties for this material are reported in Table 3, while a more detailed discussion on the reasons for this choice is provided in Appendix A.

Table 1
Properties of the constituents of the prepreg material used in the study.

MR70 carbon fibre		
[a]Diameter	μm	5.0
[a]Density	g/cm³	1.82
[a]Axial Young's modulus	GPa	325
[b]Transverse Young's modulus	GPa	25
[b]Axial shear modulus	GPa	10
[b]Axial Poisson's ratio	–	0.2
[b]Transverse Poisson's ratio	–	0.22
[a]Longitudinal tensile strength	MPa	7000
TP402 epoxy resin		
[a]Density	g/cm³	1.21
[a]Young's modulus	GPa	3.44
[b]Poisson's ratio	–	0.35
[a]Tensile strength	MPa	62

[a]Technical datasheet [48,49].
[b]Assumed from experience or literature on similar materials.

Table 2
MR70/TP402 ply properties used in the study. Footnotes indicate how we obtained each property.

MR70/TP402 ply		
[a]Density	g/cm³	1.545
[a]Longitudinal compressive modulus, E_{1c}	GPa	153
[b]Transverse moduli, $E_2 = E_3$	GPa	9.55
[c]Shear moduli, $G_{12} = G_{13}$	GPa	4.39
[b]Transverse shear modulus, G_{23}	GPa	3.54
[d]Poisson's ratios, $v_{12} = v_{13}$	–	0.26
[d]Transverse Poisson's ratio, v_{23}	–	0.50
[e]Longitudinal compressive strength, X_c	MPa	1850
[a]Longitudinal tensile strength, X_t	MPa	3880
[f]Transverse compressive strength, Y_c	MPa	160
[f]Transverse tensile strength, Y_t	MPa	40
[f]In-plane shear strength, S_l	MPa	63

[a]Rule of mixtures (E_{1c} corrected to account for typical compressive/tensile moduli difference [50]).
[b]Halpin–Tsai formulas
[c]Cylindrical assemblage model, matrix dominated [51].
[d]Periodic microstructure model [51].
[e]Back-calculated from in-house uniaxial compression tests on MD coupons.
[f]Assumed from experience or literature on similar materials.

Table 3
Material properties of Rohacell © RC200SL, as per product datasheet [52].

RC200SL		
Density, ρ	g cm⁻³	0.205
Compressive modulus, E_c	GPa	0.37
Shear modulus, G	GPa	0.123
Compressive strength, X_c	MPa	9.6
Tensile strength, X_t	MPa	10.4
Shear strength, S_l	MPa	4.8

Relevant literature suggests that a crack arrest due to the inhomogeneity effect can be obtained if the modulus and strength ratios of the microstructure (properties of the soft/weak region divided by those of the stiff/strong one) are 0.20 and 0.30, respectively, or lower [44,53]. We considered a quasi-isotropic (QI) laminate, namely $[45/90/-45/0_2/45/90/-45]_{10S}$, as our *Baseline*. We then designed the *Bio-inspired* (or *Bio* hereafter, for the sake of brevity) laminate configuration by doubling the thickness of the load bearing 0° material, but replacing half of its width with PMI foam strips, Fig. 4. It is worth noticing that such thickness increase was obtained by doubling the number of 0° plies and using the same prepreg material, in order to prevent any effect on compressive strength caused by differences in microstructural uniformity arising from the use of prepregs with different FAW [54].
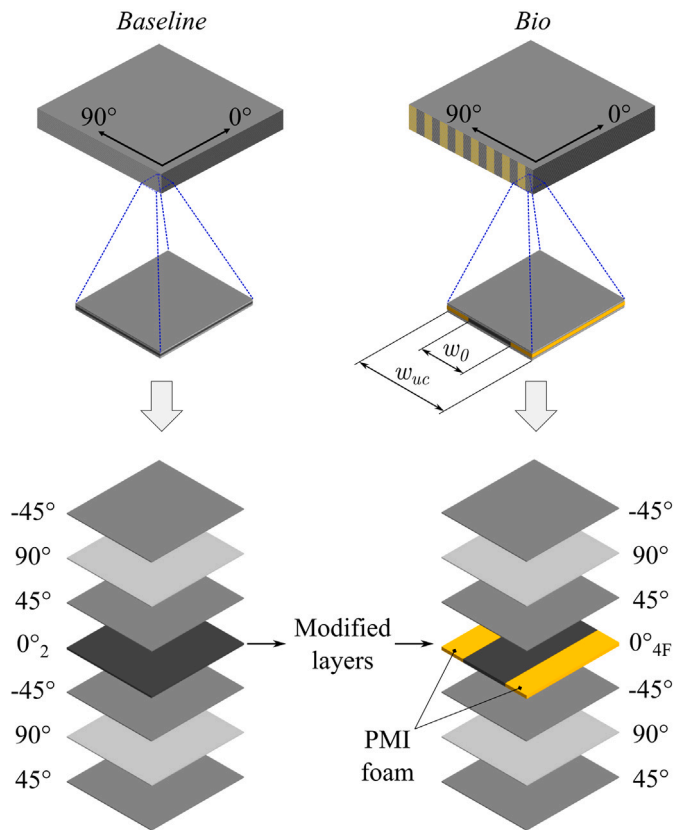
Fig. 4. Schematic representation comparing one repetitive unit of the *Baseline* and of the *Bio-inspired* laminates designed for this study. At the bottom of the image, an exploded view highlights the difference in the 0° layers.

We chose the width of foam and 0° CFRP strips, w_f and w_0 respectively in Fig. 4, based on the following. Narrow strips are desirable to achieve overall laminate homogeneity and to increase the number of soft regions that could promote crack blunting/arresting; also, narrow 0° CFRP strips imply low energy release when each single one fails, which would make the failure process more stable. At the same time, however, narrow strips make manufacturing extremely challenging and increase the risk of interaction between stiff regions: if the soft region is too narrow, off-axis plies may be able to transfer significant load between a failed 0° CFRP strip and the neighbouring ones. Typically, for CFRPs, the kinkband width (length of the kinked region in fibre direction) is estimated to be in the range of 3–25 times the fibre diameter [55]. For the material used in this study, this corresponds to 25-125 μm. We considered a width of 0.5 mm, i.e. four times the kinkband width, as a safe minimum value for the strips width. On the other hand, larger strips are easier to manufacture and guarantee even better isolation of the 0° CFRP material. However, they imply larger energy release at failure (which can be especially problematic when testing small specimens, where load redistribution is simply not possible). Eventually, we chose a value of w_f and w_0 equal to 1 mm, as a good compromise between the aspects mentioned above. We thus created the desired pattern of in-plane longitudinal alternated regions with changing stiffness and strength, while keeping the amount of structural material identical in the *Baseline* and in the *Bio* laminates.

We can identify, in the *Bio* laminate, stripe-shaped regions of two types: one fully composed by CFRP (equivalent to a $[45/90/-45/0_4/45/90/-45]_{10S}$ laminate), and one with CFRP in off-axis plies and PMI foam replacing 0° plies (equivalent to a $[45/90/-45/RC200SL_4/45/90/-45]$ hybrid laminate). We used Classic Lamination Theory (CLT) [51] and the LaRC05 [56] failure criterion to estimate the equivalent

longitudinal modulus and First Ply Failure (FPF) strength (under longitudinal uniaxial compressive load) of the two regions; the in-situ effect was accounted for by computing in-situ strengths of each ply according to established models [56–58]. We found the modulus and FPF strength ratios (soft region over stiff region) to be 0.20 and 0.28, respectively, which suggests that the designed microstructure could highly benefit from the inhomogeneity effect, as desired.

3. Manufacturing and testing

3.1. Manufacturing

Following the discussion in Section 2.2, we manufactured the two following plates, 100 mm wide and 75 mm long:

- *Baseline* plate: $[45/90/-45/0_2/45/90/-45]_{10S}$;
- *Bio* plate: $[45/90/-45/0_{4F}/45/90/-45]_{10S}$, where 0_{4F} designates the layers containing strips of foam, as described in Section 2.2.

For both plates, we used a pins and holes reference system to ensure the best possible alignment during layup [25,29]. To lay up the *Baseline* plate, we cut plies to the desired size and orientation with a CNC ply cutting machine and then followed standard lay-up practices. To manufacture the *Bio* plate, we developed a multi-step bespoke procedure, schematically summarised in Fig. 5, consisting in the following:

1. **Initial material preparation.** We start by cutting the PMI foam sheets (manually) and the prepreg (with a CNC ply cutter) to the desired size. Additionally, we manually cut 50 μm thick PET sheets and release film frames that will be used in the following steps;
2. **Partial ply-blocks layup.** We layup all the $[0]_4$, $[45/90/-45]$ and $[-45/90/45]$ ply blocks needed for the plate, with the same precautions as used for the *Baseline* plate;
3. **Laser micro-machining.** Using an Oxford Lasers Diode Pumped Solid State system, we micro-machine the $[0]_4$ prepreg ply blocks, the PMI foam sheets, and the PET sheets. Specifically, from the $[0]_4$ ply blocks we cut away rectangular slots that will accommodate foam strips; we cut the foam sheets and the PET sheets (which will be used as templates for accurate placement of the prepreg) with a complementary pattern;
4. **Complete ply-blocks assembling.** We assemble each complete $[45/90/-45/0_{4F}/45/90/-45]$ and $[-45/90/45/0_{4F}/-45/90/45]$ ply-block.

The complete ply-blocks are finally assembled together to obtain the whole *Bio* plate. Step 4 of the procedure described, as shown in Fig. 5, consists itself of multiple steps, namely:

(a) the micro-machined $[0]_4$ ply-block is laid on top of an off-axis plies block; a PET template is interposed to ensure precise alignment of the prepreg strips, while two release film frames are used to prevent sticking of the PET template to the prepreg;

(b) a sharp blade is used to separate the $[0]_4$ ply block into its strips and an external frame; such frame is temporarily removed (and preserved) to allow removal of the PET template and of the release film frames from the layup;

(c) the micro-machined foam sheet is then laid up; at this stage, the $[0]_4$ prepreg strips act as a template, guiding foam strips to precisely fill the gaps between them;

(d) the foam sheet is separated into its strips and an external frame; this latter is removed and only the strips are left on the layup;

(e) the $[0]_4$ ply-block frame, originally removed in step (b), is placed back on the layup. Hence, a complete $[0]_{4F}$ layer has been created; the complete repetitive ply-block of the *Bio* plate ($[45/90/-45/0_{4F}/45/90/-45]$ or $[-45/90/45/0_{4F}/-45/90/45]$) are obtained by just laying the missing partial off-axis ply block.
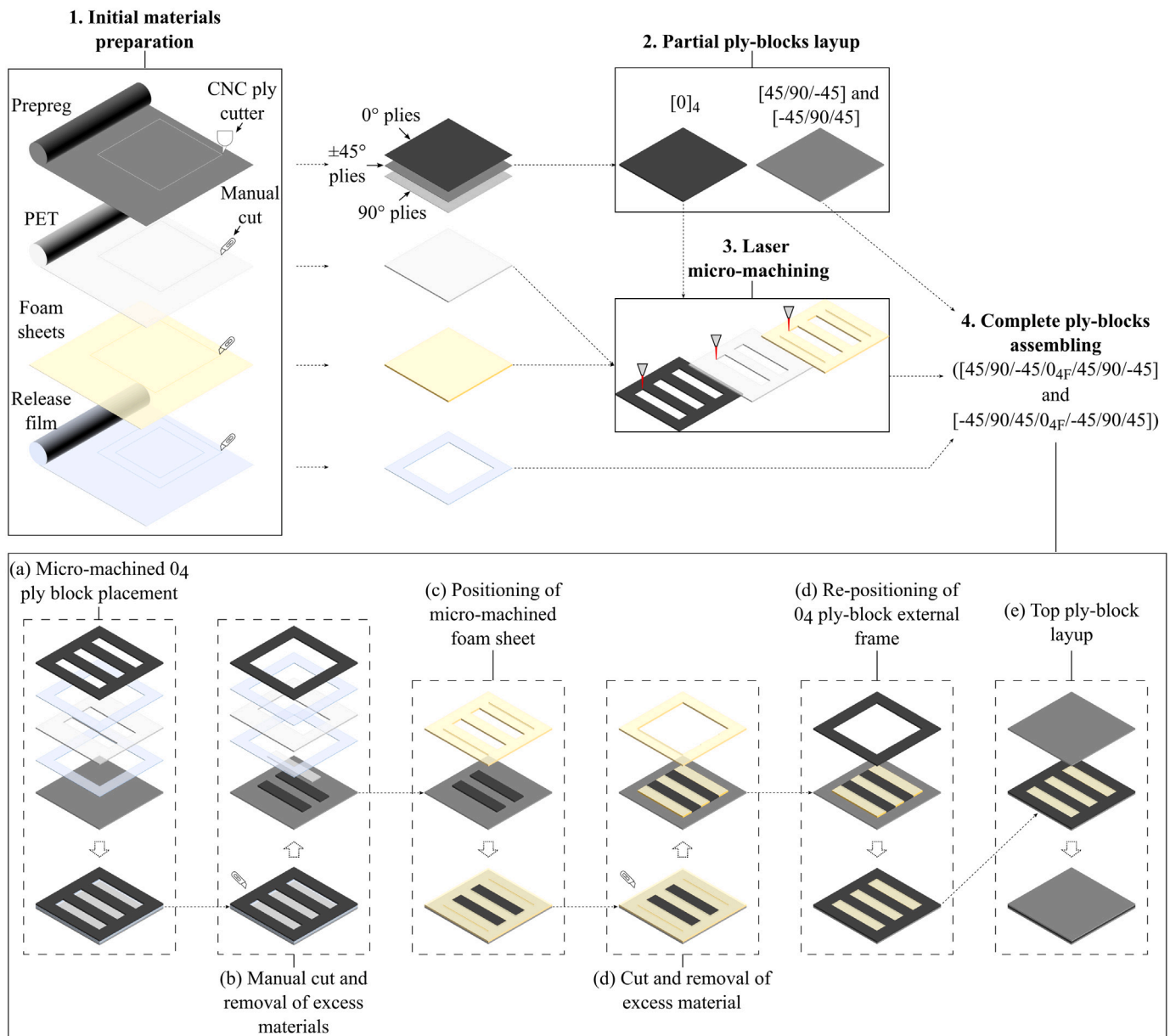
1. Initial materials preparation

CNC ply cutter

Prepreg

0° plies

±45° plies

90° plies

PET

Manual cut

Foam sheets

Release film

2. Partial ply-blocks layup

[0]₄

[45/90/-45] and [-45/90/45]

3. Laser micro-machining

4. Complete ply-blocks assembling
([45/90/-45/0₄F/45/90/-45] and [-45/90/45/0₄F/-45/90/45])

(a) Micro-machined 0₄ ply block placement

(b) Manual cut and removal of excess materials

(c) Positioning of micro-machined foam sheet

(d) Re-positioning of 0₄ ply-block external frame

(d) Cut and removal of excess material

(e) Top ply-block layup

Fig. 5. Schematic representation of the *Bio* laminate manufacturing procedure.

A video recording of the actual executions of steps (a)–(e) described above is available in the Supplementary Information. Both plates were autoclave cured according to the cycle recommended by the manufacturer [49], at a pressure of seven bars.

We verified the results of the manufacturing using 2D X-ray scans (with an Elektron Technology Xpert-80 X-ray Scanner) and optical microscopy; Figs. 6 and 7 illustrates the results. From the top view X-ray scan of the *Bio* plate in Fig. 6, where dark regions correspond to regions containing foam strips, it can be seen that a very precise longitudinal alignment of the strips has been achieved; furthermore, the sharp transition between dark and bright (full composite) regions suggests that a good through-the-thickness alignment has been achieved as well. This is confirmed by the wide view transverse cross section (A–A), and the detail micrograph (detail D) in Fig. 6. Finally, sections B–B and C–C in Fig. 6 show longitudinal cross-sections of the *Bio* plate, taken in full composite region and in a region containing foam strips, respectively. It is worth mentioning that, as is evident in detail D and section C–C of Fig. 6, the typical cell dimensions of RC200SL are comparable with the thickness of the sliced sheets used for this study. Consequently, despite

RC200SL being a closed-cell foam material, because of the slicing to ultra-thin sheets, the vast majority of its cells were open; this allowed epoxy resin to flow within the foam strips during curing and fill the volume originally occupied by air. This led to the *Bio* plate having a density of 1.35 g/cm³, against an expected value of around 1.25 g/cm³ (for comparison, the measured density of the *Baseline* plate was 1.52 g/cm³, very close to the expected value of around 1.55 g/cm³). For comparison, Figs. 7 shows a micrographs of the longitudinal cross section of the *Baseline* plate.

3.2. Testing

3.2.1. Specimens configurations and manufacturing

In order to assess the capability of the designed microstructure to deal with compressive damage initiation and propagation, we designed a small-scale notched specimen to be tested under compression, as sketched in Fig. 8. The presence of a notch ensures that damage will initiate and progress from its tip, enabling direct observation during the test and preventing issues typical of unnotched configurations
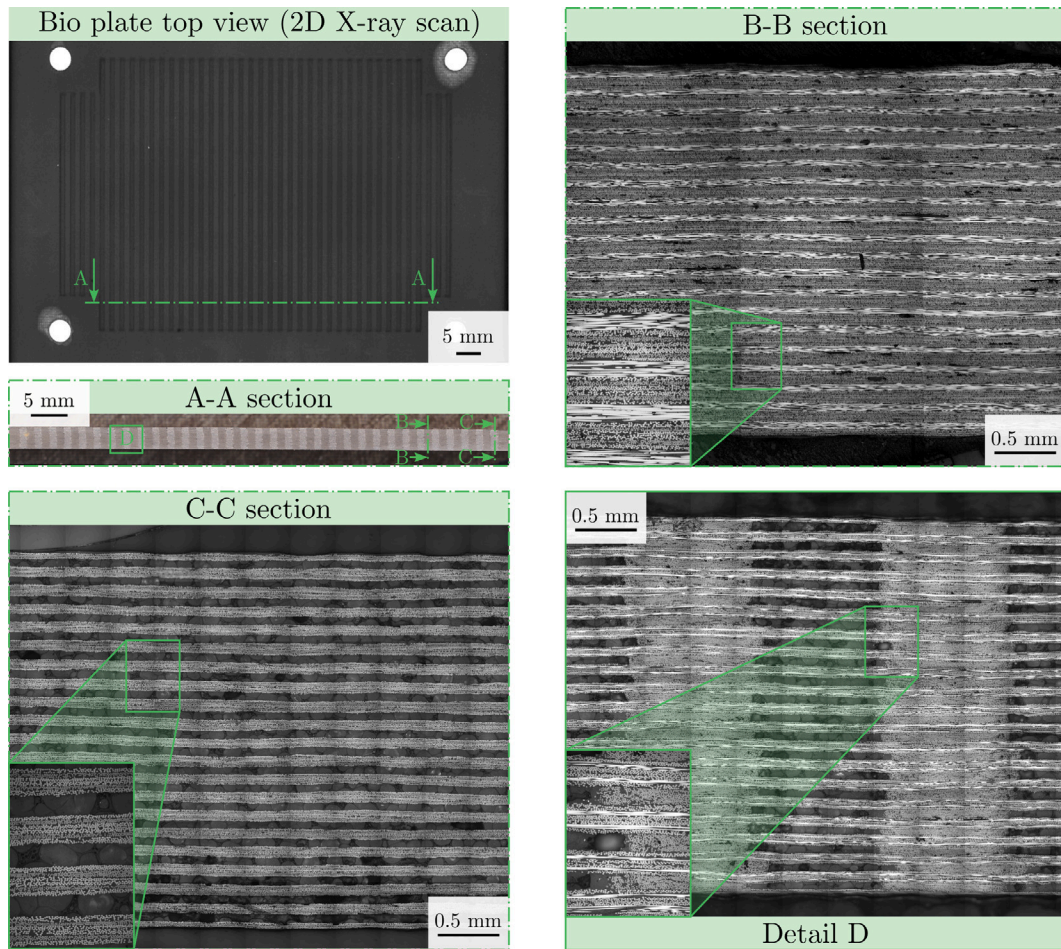
Fig. 6. *Bio* plate: 2D X-ray scan of the entire plate manufactured, a wide-view transverse cross section of the plate (A-A), a detailed micrograph of the transverse cross-section (detail D) and longitudinal cross sections taken in a full composite region (B-B) and in a region containing foam strips (C-C).
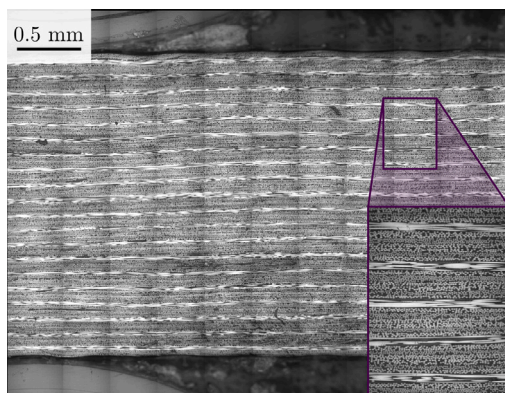

Fig. 7. *Baseline plate*: micrograph of the longitudinal cross section.

Table 4
Measured specimens dimensions and relative standard deviation.

	Ligament length, l [mm]	Specimen thickness, t [mm]	Density, ρ [g/cm^3]
Baseline	5.92 ± 0.08	2.42 ± 0.02	1.52
Bio$_f$	5.97 ± 0.08	3.01 ± 0.01	1.35
Bio$_c$	5.64 ± 0.12	3.02 ± 0.02	1.35

(edges effects, crushing at loaded ends, sudden catastrophic failure and obliteration of fracture surfaces). Additionally, it lowers the initiation and maximum loads, which, along with the small specimen size, is an essential requirement to perform in-situ tests with a micro-testing device, see Section 3.2.2. Specifically, we chose the nominal ligament length l to be equal to 6 mm, in order for it to be an integer multiple of the width of a repetitive unit cell of the designed microstructure, w_{uc}: this guarantees that specimens from the *Baseline* and *Bio* plates have the same amount of CFRP material in the ligament section. We

chose the nominal height and width, h and w respectively, to be both 10 mm. To obtain the specimens, the material was cut from the plates using a band saw; then, the top and bottom face of each specimen (those in contact with the loading platens) were ground flat and parallel using a milling machine. Finally, the notch was created using a sharp diamond coated disk saw, manually controlled. From the *Bio* plate, we obtained specimens in two configurations: *Bio$_f$* specimens, having the tip of the notch terminating in a region containing foam strips, and *Bio$_c$* specimens, having the tip of the notch terminating in a full composite region. Due to the manual nature of specimen preparation, small deviations from the nominal design may be expected; hence, we measured the ligament length of all specimens with the aid of an optical microscope; the results are synthesised in Table 4 along with the thickness measurement and the already mentioned density.

3.2.2. Test methods

We tested all specimens under compression using a Deben Microtest Module equipped with a 5 kN load cell. Flat-surface jaws were used to
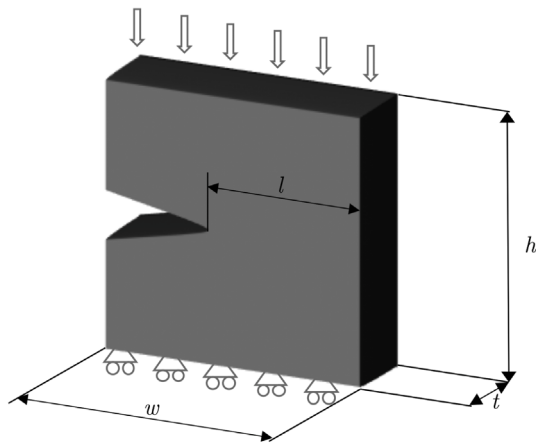
Fig. 8. Nominal geometry and loading condition of the specimens used in this study.

Fig. 9. Sample speckle pattern obtained on the small-scale notched compression specimens. The superimposed contour plot shows the pattern quality as evaluated by the DIC software GOM Correlate (green, top of the scale: high quality; red, bottom of the scale: low quality). (For interpretation of the references to colour in this figure legend, the reader is referred to the web version of this article.)

apply a relative compressive displacement to the top and bottom faces of the specimen, as shown in Fig. 8, at a controlled input displacement rate of 0.1 mm/min. Force and cross-head displacement were recorded throughout the test at 10 Hz. To gather as much information as possible, we conducted tests with different approaches:

- **In-situ SEM tests.** We prepared specimens by sputter coating a thin (2-3 nm) layer of gold on their surface, including on the notch faces and notch tip. We then loaded the testing rig, with the specimen ready for testing, inside a Hitachi S-3700N scanning electron microscope. We increased the load on the specimen and stopped at regular intervals to observe it and take pictures. Specifically, we tilted the SEM stage to be able to observe and capture damage evolution at the notch tip of the specimen.

- **Incremental tests with in-between 2D X-ray scans.** To observe sub-surface damage progression, we tested a few specimens with incremental loading steps, with in-between 2D X-ray scans. Specifically we proceeded as follows:

  1. we installed the specimen in the testing rig and loaded it to the desired level (i.e. previously reached load plus fixed increment);
  2. we unloaded the specimen and removed it from the rig;
  3. we applied an X-ray reflective penetrant liquid (Dibromoethane/Dibromomethane) to the specimen;
  4. we obtained a 2D scan of the specimen using an Elekron Technology Xpert-80 X-ray Scanner;
  5. we repeated the cycle until final failure of the specimen.

- **In-situ (optical microscope) tests for DIC analysis.** We prepared a few specimens for DIC analysis by creating a speckle pattern on their surface. Since a very localised stress concentration is expected, due to the sharp notch, we optimised, through extensive trials, our speckle pattern and DIC analysis parameters to ensure the best possible spatial resolution while retaining good accuracy. To produce the speckle pattern, we used an airbrush with a 0.5 mm nozzle and airbrush-ready, water-based, acrylic polyurethane paints; we used a working pressure of 2 bar and a spraying distance of around 10 cm, with a fixed paint flow regulation on the airbrush. Firstly, we applied a uniform layer of white paint; then, we created black speckles; we adjusted the number of black paint passes (one to three) for each case, based on pattern quality checks (average speckle size and overall coverage) performed during painting. During the tests, we recorded images at 25 frames per second with an optical Hirox microscope. Before testing, we performed lens calibration with an ad-hoc calibration target provided by the microscope manufacturer. Additionally, we
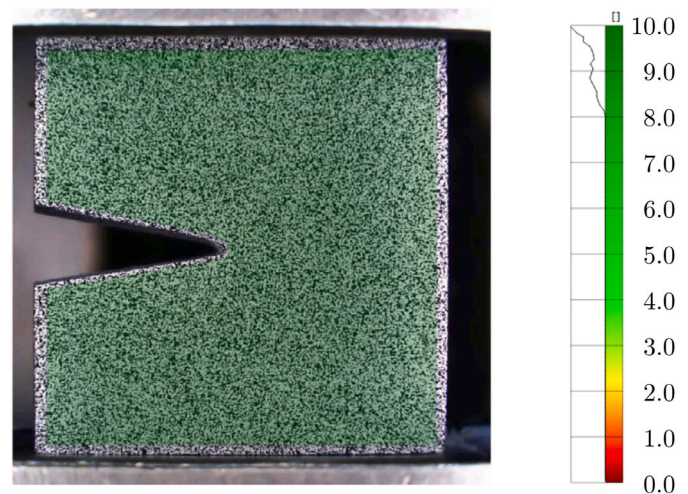
used polarising lens during all tests, as this has been shown [59] (and confirmed during our trial tests) to reduce glare and improve contrast, thus decreasing both bias and random errors. We placed the testing rig on the microscope stage and ensured that the speckled face of the specimen was perpendicular to the optical system. We analysed the images captured using the commercial software GOM Correlate; we chose a facet size of 15 pixels and a facet distance of 8 and we applied temporal filtering to reduce results noise. Fig. 9 shows a typical speckle pattern obtained, with a superimposed pattern quality contour plot, for the parameters chosen, as evaluated by the GOM Correlate software.

4. Finite element (FE) modelling

We created three simple linear elastic FE models, one per each specimen configuration, using the commercial software Abaqus 2021 [60]. We included in the models the LaRC05 failure criterion [56], with the main goal of gaining qualitative insight about the possible failure initiation mechanism occurring during testing. The geometry and loading condition of the models are as shown in Fig. 8; the notch was explicitly modelled, with a tip radius of 45 µm (corresponding to the actual average value measured from all the specimens with an optical microscope). For the Bio_c and Bio_f configurations, we assumed the tip of the notch to be exactly in the middle of the corresponding soft or stiff region, respectively. Due to the symmetry with respect to the midplane, we modelled only half of the model. We used reduced integration continuum shell elements (SC8R) to model the outer portion of the specimen and reduced integration solid elements (C3D8R), along with a fine ply-by-ply discretisation, to model the central portion, see Fig. 10. Close to the notch tip, we used a very fine mesh size (6–10 µm) to accurately capture the steep stress/strain gradient caused by the notch. We used the material properties reported in Tables 2 and 3 as input for our models; we additionally pre-processed ply strengths in Table 2 with an ad-hoc routine to assign the correct in-situ strengths (according to [56–58]) to each ply in the model.

5. Results

Fig. 11(a) presents the load displacement curves obtained from all tests conducted, colour-grouped by specimen type. Initially, all curves
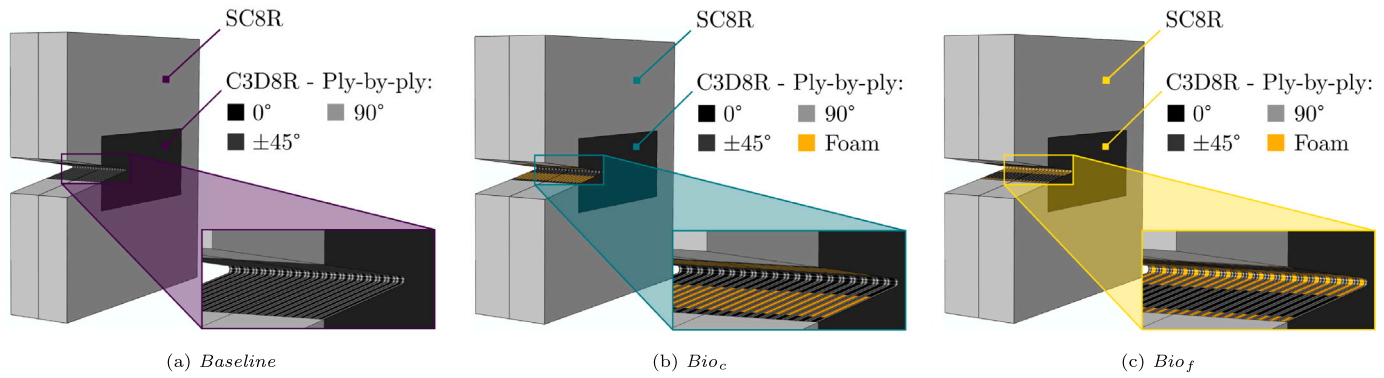
Fig. 10. Details of the three FE models built. (a) *Baseline*, (b) *Bio_c*, and (c) *Bio_f* specimens. The magnified view inserts at the bottom right of each subfigure highlight: (i) the difference between the *Baseline* specimen – ordinary CFRP with no foam inserts – and the *Bio* ones – where the original microstructure devised is evident – and (ii) the different location of the notch tip with respect to the foam inserts in the *Bio_c* and *Bio_f* specimens.
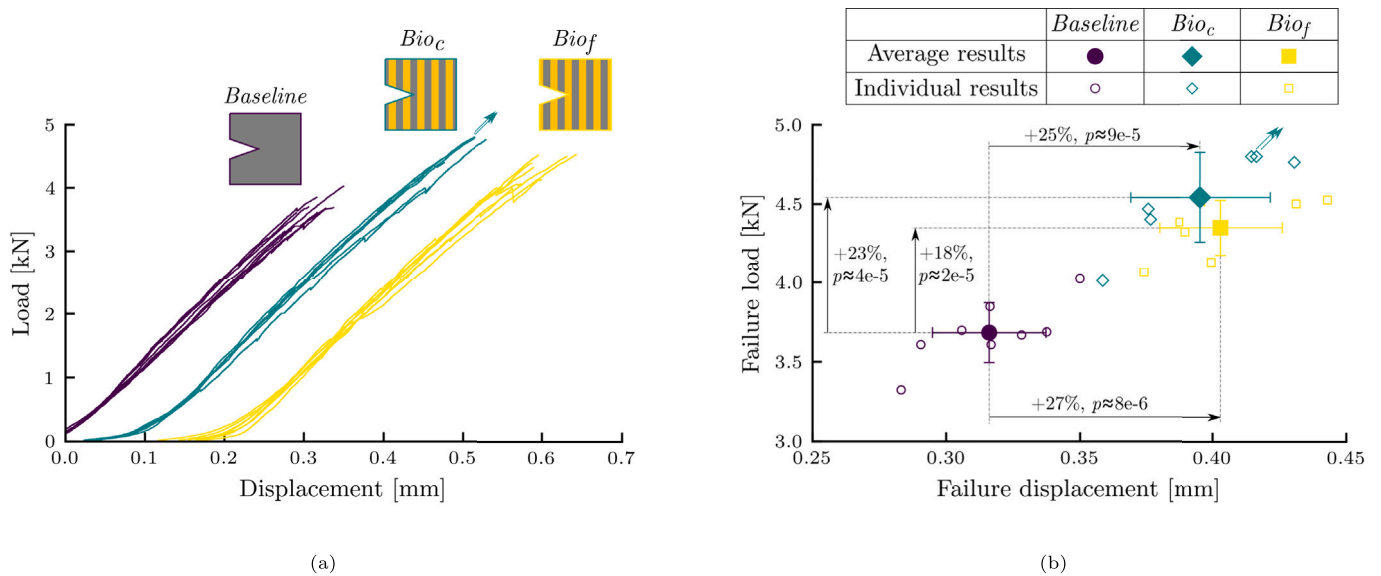

Fig. 11. (a) Load displacement curves for all specimens tested, colour-grouped by specimen type. For clarity, curves from *Bio_c* and *Bio_f* specimens have been translated by 0.1 and 0.2 mm respectively. (b) Failure load and corresponding displacement scatter plot; both individual results (single specimens) and averages for each specimen type are reported; the error bars reported around average results represent a ± 1 standard deviation interval. The percent increase in average failure load and displacement of the *Bio* specimens with respect to the *Baseline* ones are reported in the figure, along with the relevant *p*-value.

have been shifted so that their linear region would extend to the origin (to adjust for the knee caused by imperfect contact at the beginning of the tests); then, for clarity, curves from *Bio_c* and *Bio_f* specimens have been shifted to the right by 0.1 and 0.2 mm, respectively.

Among the *Bio_c* specimens, two did not fail by the time the test was stopped to prevent damage to the load cell (i.e. when reaching 4800 N); this is indicated in the plot by small continuation arrows. Fig. 11(b) presents both average values and single-specimen values of failure load versus failure displacement for the different specimen types; error bars indicate a ±1 standard deviation interval. Our results show that the increase in average failure load, when comparing to the *Baseline* configuration, is approximately 23% for *Bio_c* specimens (at least, considering that two specimens did not fail) and 18% for *Bio_f* specimens; the increases in the average value of displacement at failure are 25% and (at least) 27% for *Bio_c* and *Bio_f* specimens, respectively. To evaluate the statistical significance of these results, we tested the null hypothesis that the samples tested (*Bio_c* versus *Baseline* and *Bio_f* versus *Baseline*) have identical average expected values, by means of T-test. The *p*-value obtained quantifies the probability that the samples tested may be extracted from the same population, i.e. that the difference in the average values obtained from the samples (failure load and failure displacement increase, in our study) is not statistically

significant. Commonly, a value of 0.05 (5% probability) is assumed as threshold for statistical significance. As reported in Fig. 11(b), all the *p*-values obtained are significantly smaller than the threshold, confirming the statistical significance of the results.

Table 5 reports, for each specimen type, the average values of the failure load F_{max}, the load per unit ligament length at failure, $\frac{F_{max}}{l}$, and the ligament section average specific stress at failure, $\frac{F_{max}}{lt\rho}$; for each of these, the corresponding percent coefficient of variation is reported in parentheses; all coefficients of variation are well within typical values encountered in compression testing of composite materials [61]. Results in Table 5 show that the *Bio* microstructural design led to an increase in the average ligament section specific stress at failure, $\frac{F_{max}}{lt\rho}$, and that this increase was more pronounced when the notch tip was located in a full composite region, i.e. for *Bio_c* specimens.

Fig. 12 shows SEM pictures, taken at increasing load levels during the test, of the notch tip region of one specimen per type, up to final failure. In the *Baseline* and *Bio_c* specimens, damage is first seen at a load level of 1600 N, Figs. 12(a) and 12(b). With increasing load, material crushing for these specimens becomes more and more evident, eventually spanning the entire width of the specimens. The *Baseline*
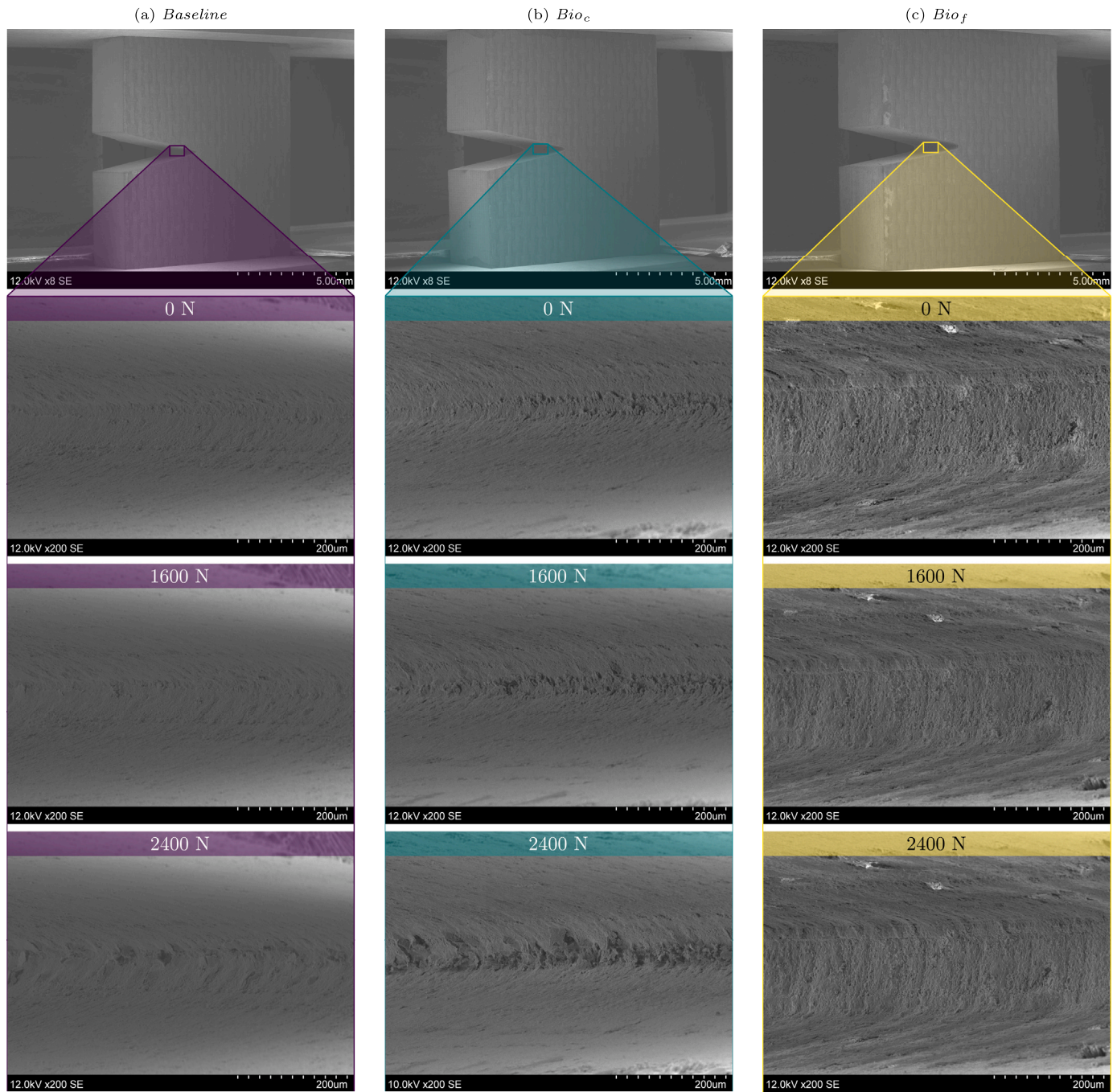
Fig. 12. (continued on next page) SEM pictures taken during in-situ testing of the different specimen types, at different load levels. (a) *Baseline* specimen, (b) *Bio_c* specimen, and (c) *Bio_f* specimen. Top images are global views of the specimens in the rig before testing; bottom images are global view of the specimens right after failure.

Table 5
Synthesis of quantitative results from the tests. Values in parenthesis represent the percent coefficient of variation of each entry.

	F_{max} [N]	$\frac{F_{max}}{l}$ [MPa mm]	$\frac{F_{max}}{lt\rho}$ [MPa cm^3 g^{-1}]
Baseline	3685 (5.1)	627 (6.1)	170 (6.1)
Bio_c	≥4542 (6.3)	≥807 (7.8)	≥198 (8.1)
Bio_f	4350 (4.0)	729 (5.2)	180 (4.9)

specimen considered failed at a load of 3600 N, while the *Bio_c* one failed at a load of 4760 N, despite the severe crushing observed at the notch tip, Fig. 12(b). In the *Bio_f* specimen, Fig. 12(c), damage at the

notch tip appears much later, being firstly visible at a load of 3200 N; subsequently it remains barely visible, even in the last image taken before failure, at a load of 4000 N. The *Bio_f* specimen considered failed at a load of 4390 N.

Fig. 13 reports results from the incremental tests with in-between 2D X-ray scans. In the *Baseline* specimen, damage propagating from the notch tip is visible after loading to 2400 N, Fig. 13(a). Stable damage propagation is observed with increasing load; the last X-ray scan performed before final failure of the specimen (after loading to 3200 N) shows damage extending from the notch tip for a length slightly larger than 1 mm. Fig. 13(b) shows the progression of damage for a *Bio_c* specimen. In this case, some damage is visible at the notch tip after loading to 2400 N; after loading at 2800 N, it becomes more
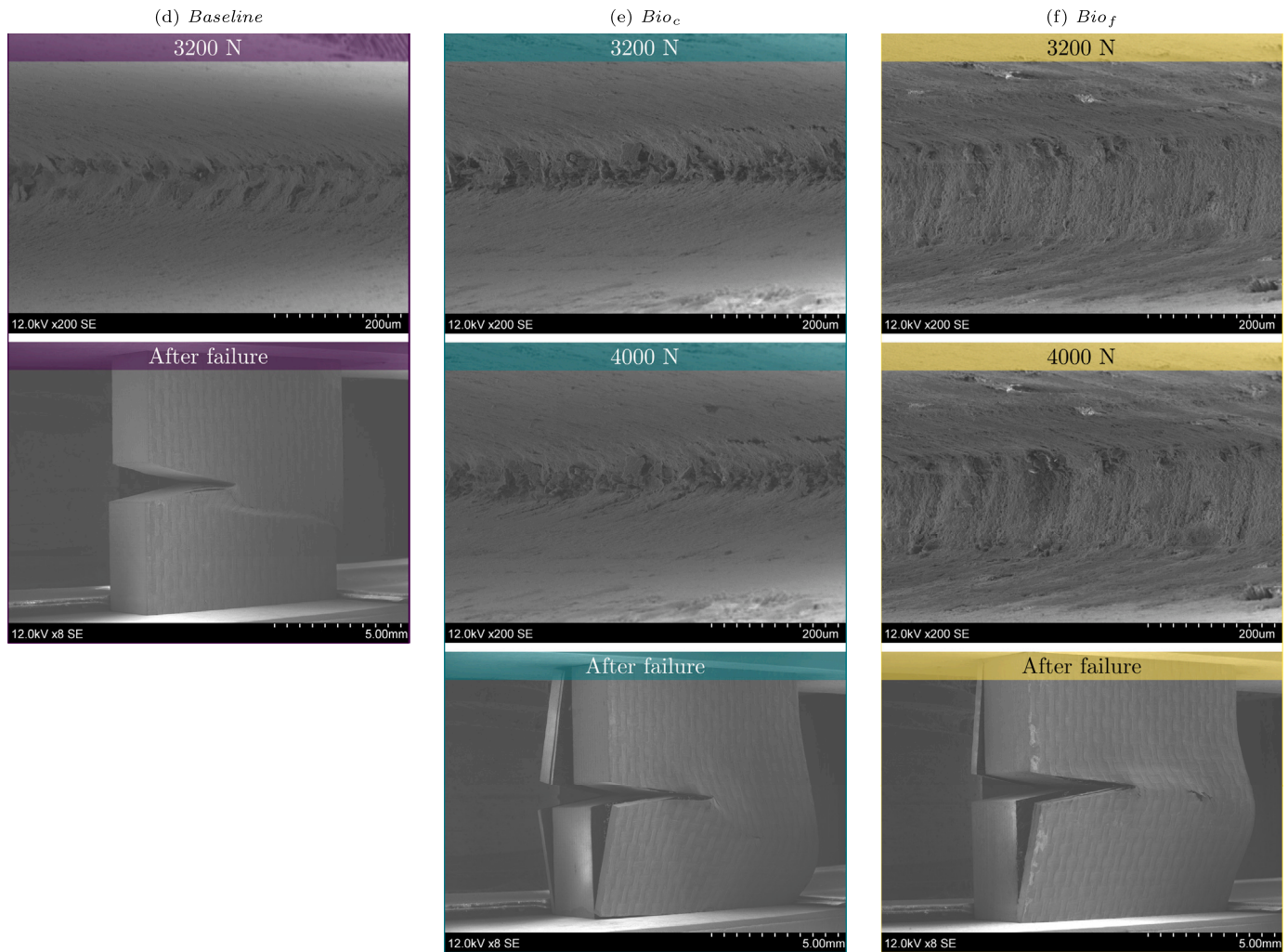
(d) *Baseline*   (e) *Bio_c*   (f) *Bio_f*

Fig. 12. (*continued*).

visible, reaching the next soft region in the specimen. From this point on, Fig. 13(b) shows that damage propagation is arrested: with further loading steps the damaged area gets brighter, more defined, and it slightly expands in the vertical direction, but no horizontal propagation is observed. Finally, Fig. 13(c) shows that, in the *Bio_f* specimen, where the notch tip is located in a soft region, no damage propagation from the notch tip was visible before final failure.

Fig. 14 shows, for one specimen of each type, longitudinal strain contour plot at increasing loads. The *Bio_c* specimen shown in Fig. 14(b) is one of the two that did not fail by the time the test was stopped to prevent damage to the load cell. Additionally, animations showing the complete evolution of the load–displacement history and of the longitudinal strain contour from DIC, side-by-side and for each specimen in Fig. 14, are provided as Supplementary Information to this paper.

6. Discussion

6.1. Manufacturing of bio-inspired MD CFRP laminates

The bespoke manufacturing procedure we developed in this work proved successful to produce the desired microstructure with an in-plane alternation of stiff and soft regions, as seen in Fig. 6. The ultra-thin sliced RC200SL sheets withstood the high temperature and pressure of the curing cycle; they conformed to the thickness of the $[0°]_4$ ply-blocks and, as a result, the thickness of the *Bio* laminate was

uniform and its surfaces were smooth. As mentioned in Section 3, most cells in the foam strips were open and allowed epoxy resin to flow in during curing. We speculate here that the use of a foam material with finer cell dimensions (e.g. RC110RIMA, as shown in Fig. 15) could prevent this, leading to a significantly lower density of the laminate and hence much better specific properties.

In addition, the presence of large, opened cells caused an abundance of air trapped in the plate during manufacturing. This resulted in the *Bio* laminate containing more voids than the *Baseline* one, as seen in Figs. 6 and 7. We observed relatively large voids at the boundaries between RC200SL and $[0°]_4$ strips, as visible in Fig. 6. Voids are detrimental to mechanical properties, especially in compression [3]. Therefore, we recommend that the use of finer cells foam materials be taken into consideration for future studies, as this may have a twofold beneficial effect by: (i) reducing the specific weight of the plates, thus improving specific properties and (ii) guaranteeing a more uniform microstructure with a significantly lower volume of voids, and hence better mechanical properties.

6.2. On the failure process of the specimens tested

6.2.1. FE results

For both the *Baseline* and *Bio_c* specimens, the first FI predicted to reach the critical value of one is that for fibre kinking, specifically in 0° plies and in proximity of the notch tip. While the load at which
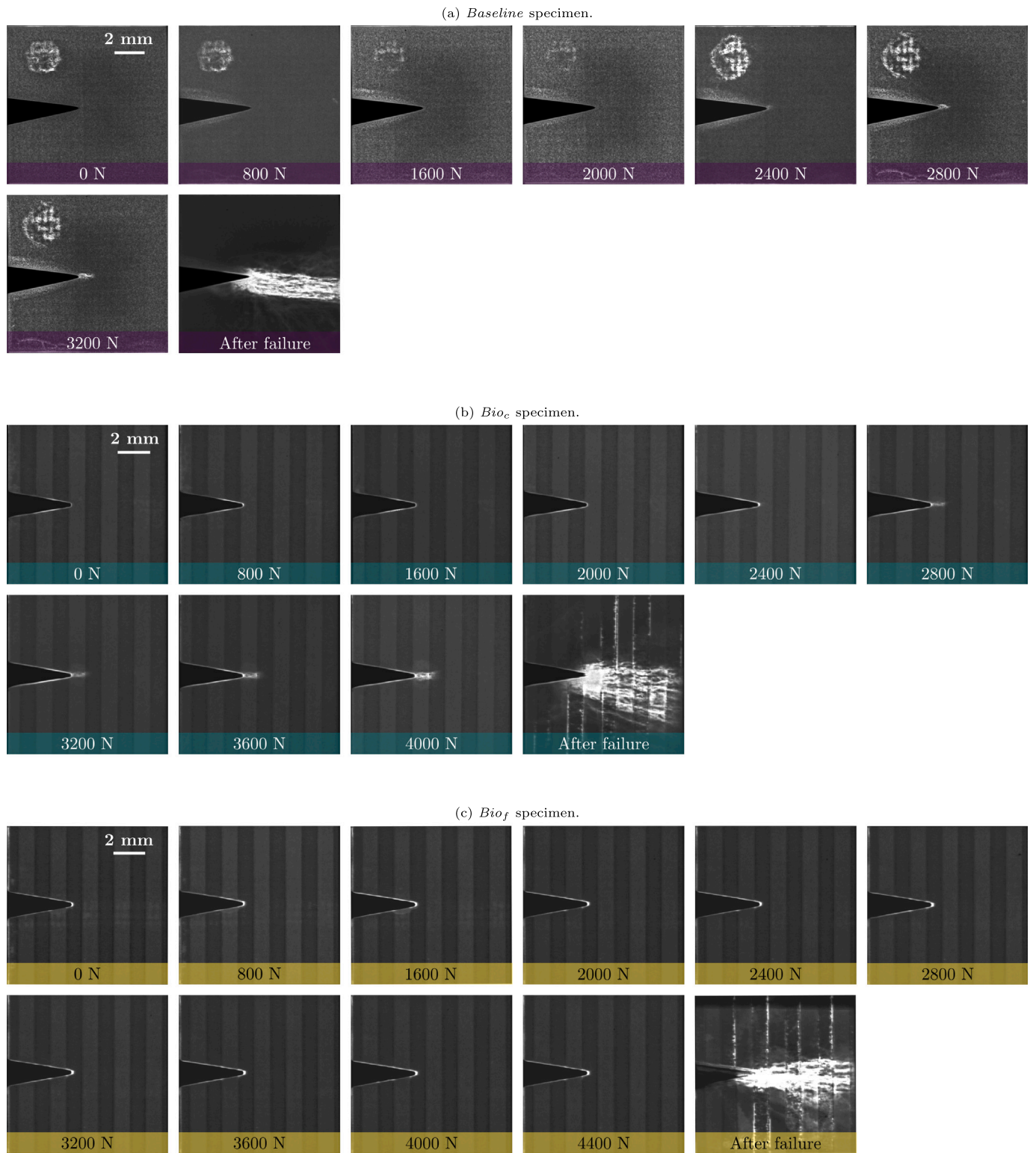
(a) *Baseline* specimen.

(b) *Bio$_c$* specimen.

(c) *Bio$_f$* specimen.

Fig. 13. Front view 2D X-ray scans of specimens (one per type) taken after loading at incremental levels, up to final failure. (a) *Baseline* specimen, (b) *Bio$_c$* specimen, and (c) *Bio$_f$* specimen.

this happens is lower than that at which damage is first observed in Figs. 12(a) and 12(b) (this seems sensible considering that the failure location is highly constrained in our specimens), the model os able to finely capture the mechanisms involved and the locations of damage initiation. This is shown in Fig. 16, which displays the contour plot of the FI for fibre kinking/splitting at the notch tip of the *Baseline* model; a magnified view of the region around the symmetry plane of the specimen is provided and compared with an SEM picture of a *Baseline*

specimen taken at exactly the same location during in-situ testing. The model predicts the critical locations, in each pair of adjacent 0° plies, to be slightly offset from the ligament section, due to the influence of the neighbouring +45° or −45° ply; this matches closely with what can be observed in the SEM picture.

In the case of the *Bio$_f$* model, no 0° ply exists at the notch tip, because of it being located in a soft region, see Fig. 10(b). Consequently, the first FI to reach the value of one is again that for fibre
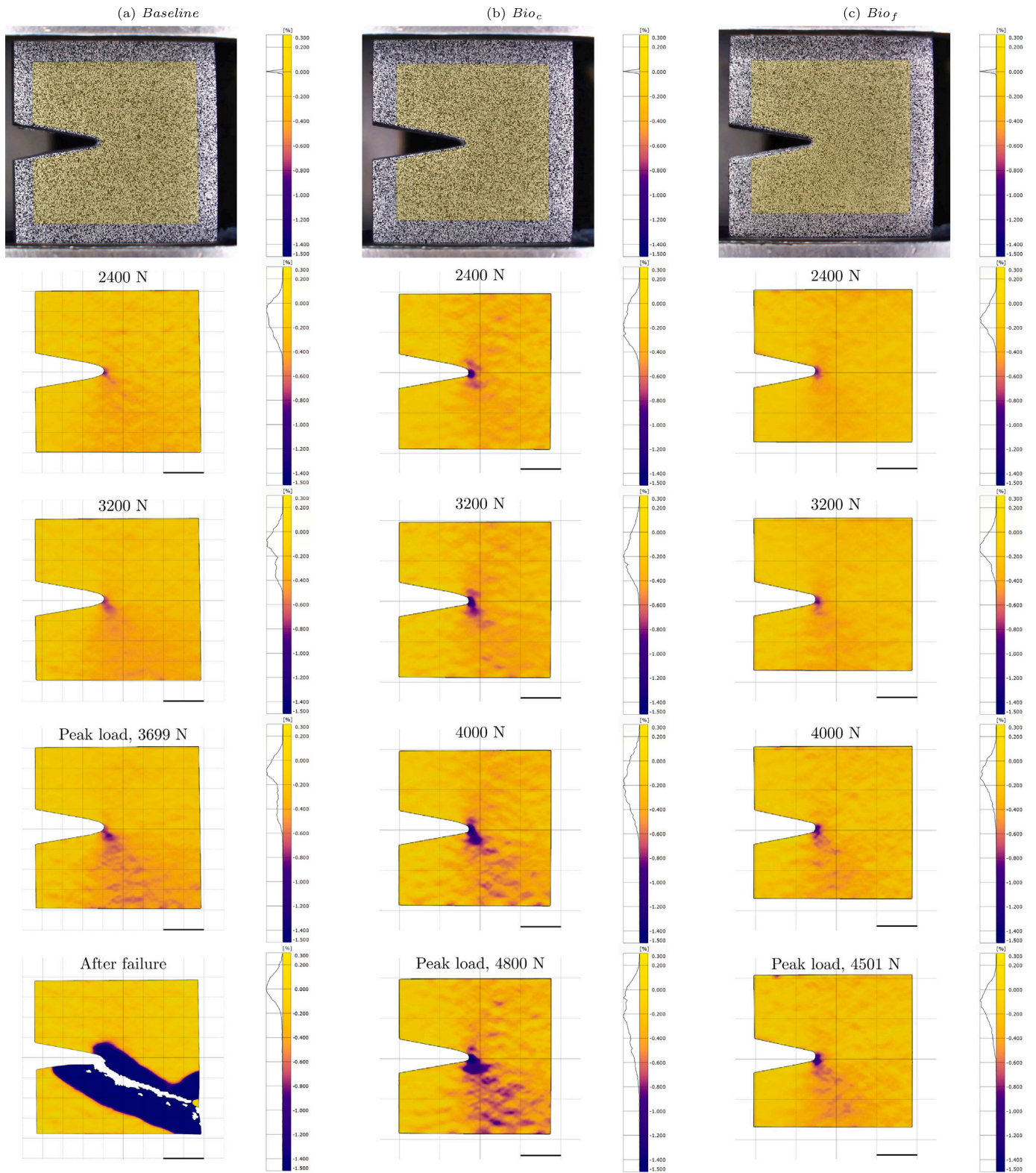
Fig. 14. Longitudinal strain contour plots, as obtained by DIC, at different load levels: (a) *Baseline* specimen, (b) *Bio$_c$* specimen, and (c) *Bio$_f$* specimen. For each subfigure, the top image shows the actual specimens and, superposed, the region of interest selected. The scale bar at the bottom right of each contour plot corresponds to a length of 2 mm.

kinking/splitting, but in off-axis plies. Once again, this is found to happen at a load lower than that at which damage is first observed in Fig. 12(c), but higher than that at which a FI equal to one is obtained in the FE analyses of the *Baseline* and the *Bio$_c$* specimens, qualitatively agreeing with what observed experimentally.

6.2.2. Baseline specimens

During tests of the *Baseline* specimens, as reported in Section 5, we observed damage initiating from the notch tip and propagating stably before final failure occurred. From the in-situ SEM observations, Fig. 12(a), and the FE results discussed in Section 6.2.1, the first
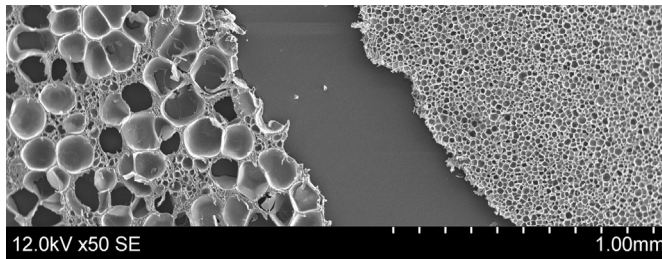
Fig. 15. SEM image showing 70 μm thick sheets of RC200SL (left) and RC110RIMA (right). RC200SL shows much larger cells, most of which are open (due to the material being sliced to such a thin sheet).
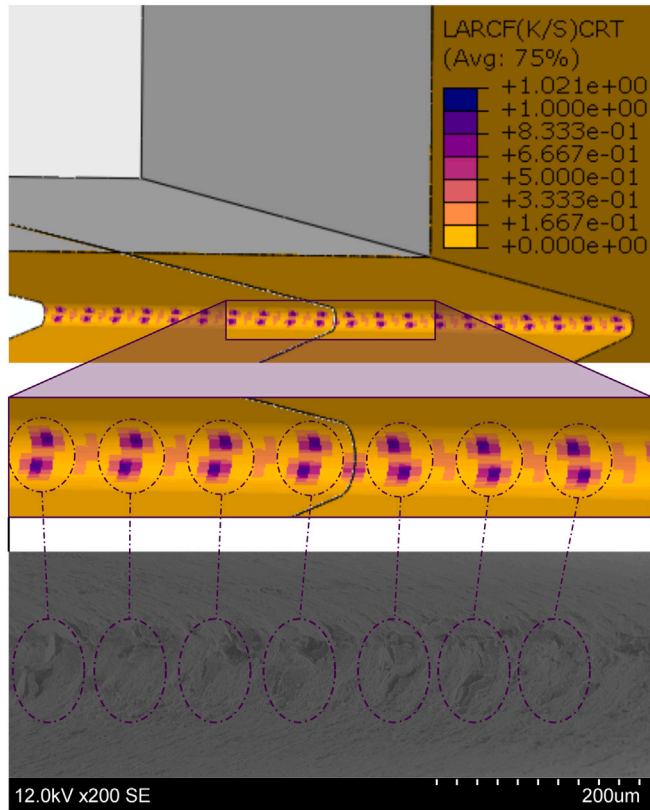

Fig. 16. Contour plot of the FI for fibre kinking/splitting at the notch tip of the *Baseline* FE model, and comparison of a portion of it with an SEM picture taken at the same specimen location during an in-situ test: a clear correspondence between the damage visible in the SEM picture and the predicted critical locations in the FE results can clearly be seen.

damage mechanism to occur appears to be 0° fibre microbuckling into the free surface of the notch tip; this is a typical feature of compression loaded composites having stress raisers like holes or notches. With increasing load, X-ray scans show stable damage propagation within the specimen, Fig. 13(a). No 0° or ±45° ply splits are visible in Fig. 13(a), and no damage was visible on the surface plies (+45°) of the specimens during testing; this strongly suggests that the damage observed in X-ray scans is likely due to kinkband propagation in 0° plies. This can be justified by the fact that the high in-situ strength of the ultra-thin ply material helps preventing ply splitting, while the reduced delamination tendency helps preventing catastrophic failure due to interaction between delamination and fibre kinking. The development of internal damage prior to failure in *Baseline* specimens is also confirmed by longitudinal strain contour plots obtained from DIC, Fig. 14(a): a region of strain concentration is seen to progress, with increasing load,

from the tip of the notch towards the bottom right of the specimen, anticipating the path of the final failure, as seen in the very last frame in Fig. 14(a).

6.2.3. *Bio_c* specimens

The *Bio_c* specimens present an initial behaviour similar to that observed in the *Baseline* ones, with damage appearing early in the test, mostly in the form of 0° fibre microbuckling into the free surface of the notch tip and overall crushing, Fig. 12(b). In this case too, stable damage propagation is observed in the X-ray scans taken during incremental load testing of a *Bio_c* specimen, Fig. 13(b): damage propagates through the entire stiff strip of material and reaches the following soft region, at a load of 2800 N; at this point, no ply splits are observed, suggesting kinkband propagation in 0° plies may be the main damage mechanism occurring. As mentioned in Section 5, however, subsequent X-ray scans show that damage propagation along the ligament sections is prevented by the presence of the soft region, confirming the potential of the designed microstructure to arrest a propagating compressive crack. X-ray scans taken after loading at 3200, 3600 and 4000 N show an increasing brightness in the initial damage region, which can be associated with increasingly severe local damage (possibly progressively involving off-axis plies too), and a halo developing around it, suggesting the onset of delamination. This sequence of events matches observations obtained from in-situ SEM tests, as shown in Fig. 17 (note that delaminations are visible also in the central region of the specimen at a load of 4000 N, Fig. 12(b). Delamination onset may have been triggered by in-plane fibre kinking turning to out-of-plane kinking with increasing load; furthermore it may have been facilitated by the presence of voids, as discussed in Section 6.1. It is therefore even more impressive that the *Bio_c* specimens were able to withstand much higher load than the *Baseline* ones, even in the presence of delaminations. This is evident also in Fig. 14(b), where the specimen used for DIC analysis was able to withstand a load of 4800 N without failing, despite the overall high strain reached and the presence of damage as understandable by the large strain concentration region extending from the notch tip.

6.2.4. *Bio_f* specimens

Bio_f specimens behaved in a different way with respect to both *Baseline* and *Bio_c* specimens. Specifically, they tended to not develop extensive damage, or to develop just minimal damage, prior to final failure. This was seen consistently in in-situ SEM testing, where only minor damage at the notch tip was observed, Fig. 12(c), and in incremental tests with X-ray scans, where no damage propagation from the notch tip was observed, Fig. 13(c). Also, observing results from DIC, Fig. 14(c), we can see how a very localised region of high strain exists at the tip of the notch; with increasing loads, this region barely expands along the ligament sections, but rather extends slightly along the loading direction, even for loads as high as 4500 N. This suggests that no damage is initiating and propagating from the notch. The soft region is able to undergo larger deformation than those a stiffer region would, and thus it effectively blunts the effect of the presence of the notch, alleviating the stress on the next stiff region.

6.3. On the improvement of compressive performance obtained with the bio microstructure

As demonstrated by Fig. 11, the novel microstructural concept presented in this work led to a significant improvement of compressive performance, in terms of load bearing capabilities in presence of a stress raiser, when compared to a typical industrially-relevant CFRP laminate. More importantly, these gains exceeded the weight penalty (+10%) caused by the introduction of a significant volume (+25%) of non-structural material, and led to an improvement even when considering specific average ligament stress at failure, as seen in Table 5. Notably, this was achieved despite a sub-optimal choice of the foam material used, as discussed in Section 6.1; this suggests that further room for
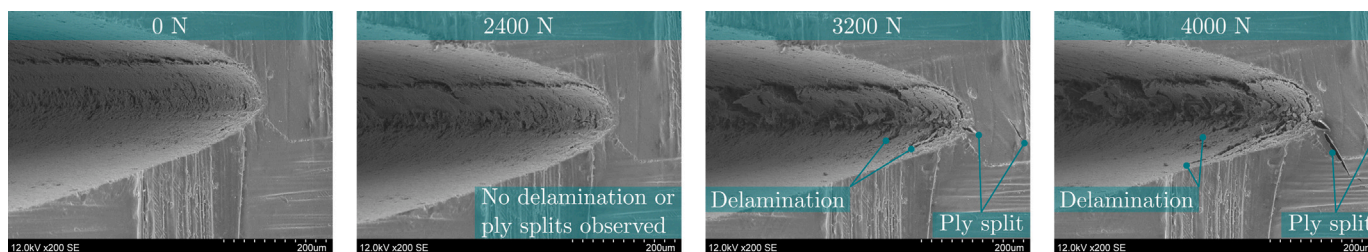
Fig. 17. Sequence of SEM pictures taken at increasing loads during testing of a *Bio_c* specimen. At high loads (≥3200 N), 45° ply splits and delaminations appear.

improvement exists. Additionally, simple calculations as those reported in Appendix A show that the concept proposed brings improvements also for stiffness-driven design of least weight composite plates. These two aspects make the developed microstructure a strong candidate for adoption in the design of lightweight structures. Experimental studies to systematically study the behaviour and performance of the proposed concept at the coupon level, especially in terms of apparent fracture toughness (e.g. using compact compression test, [62]) will be invaluable.

7. Conclusions

In this work, we have designed, manufactured and tested the first bio-inspired microstructure aimed at improving in-plane compressive performance of MD CFRP laminates. The concept we propose exploits design strategies learned from natural layered materials with excellent fracture properties, such as the anchoring spicula of the deep-sea glass sponge *M. chuni*. Specifically, we created in the laminate an in-plane alternation of stiff (and strong) and soft (and weak) regions by embedding load-aligned PMI foam strips in the load bearing 0° plies. In order to manufacture the novel microstructure, we developed a bespoke multi-step manufacturing procedure, which exploits precision laser micro-machining and tailored alignment strategies (a pin-and-hole system and purposely laser-machined PET templates) to guarantee optimal results. We assessed the performance of the microstructure by testing small-scale notched specimens under compression and comparing the results with those of a comparable, industrially relevant, MD CFRP laminate. Our test results show that:

- the novel bio-inspired microstructure led to a statistically significant increase in final failure load and displacement. Specifically, the failure load was increased by either 18% or 23%, depending on the initial location of the notch tip in the specimens;
- the increase in failure load more than compensated the increase in weight caused by the introduction in the laminate of the soft, non-load-bearing, phase. In other words the average ligament section specific stress at failure was increased by the adoption of the novel bio-inspired microstructure;
- when the notch tip was located in a soft region, initiation of compressive damage was delayed or completely avoided, suggesting that a strong blunting effect was achieved in this configuration;
- when the notch tip was located in a stiff region, damage initially developed and propagated in a similar way to what observed in *Baseline* specimens. However, when it reached a soft region, the propagating compressive crack was arrested until final failure, which occurred at loads much higher than for the *Baseline* specimens.

Simple analytical considerations also show that the proposed microstructural concept would bring advantages for stiffness-driven design of least weight composite plates.

Overall, the original bio-inspired concept proposed in this paper holds the potential to improve significantly the response under compression and the damage tolerance of composite structures, and hence to have a substantial industrial impact.

CRediT authorship contribution statement

Torquato Garulli: Conceptualization, Methodology, Formal analysis, Investigation, Writing – original draft, Writing – review & editing, Visualization. **Tomas J. Katafiasz:** Investigation, Writing – review & editing. **Emile S. Greenhalgh:** Conceptualization, Methodology, Resources, Writing – review & editing, Supervision, Funding acquisition. **Silvestre T. Pinho:** Conceptualization, Methodology, Resources, Writing – review & editing, Supervision, Funding acquisition.

Declaration of competing interest

The authors declare that they have no known competing financial interests or personal relationships that could have appeared to influence the work reported in this paper.

Data availability

Data will be made available upon reasonable request.

Acknowledgements

Appendix A. On the choice of the material for the soft inclusions

The material to be adopted for the soft strip insertions in the load bearing layers of the novel microstructure must comply to manufacturing constraints, both in terms of feasible geometry (it must be available or workable to the desired shape, possibly without major complications) and of processing compatibility (it must withstand the typical curing conditions of the base CFRP material, i.e. high temperatures up to 135 °C and pressuer up to seven bars). Among materials satisfying these requirements, polymer matrix materials, polymeric foams and FRPs are the most appealing solutions. FRPs do not actually fit the idea of a much softer material (when compared to the base CFRP material), and would not be adequate to obtain a significant inhomogeneity effect, but we included them in the following analysis for the sake of interest. Table A.6 lists the materials considered, along with their relevant properties, namely:

- two PMI foam materials: Rohacell© 110RIMA and Rohacell© 200SL;
- two common polymer matrix materials, one thermoplastic (PEEK) and one thermoset (a typical epoxy) material;
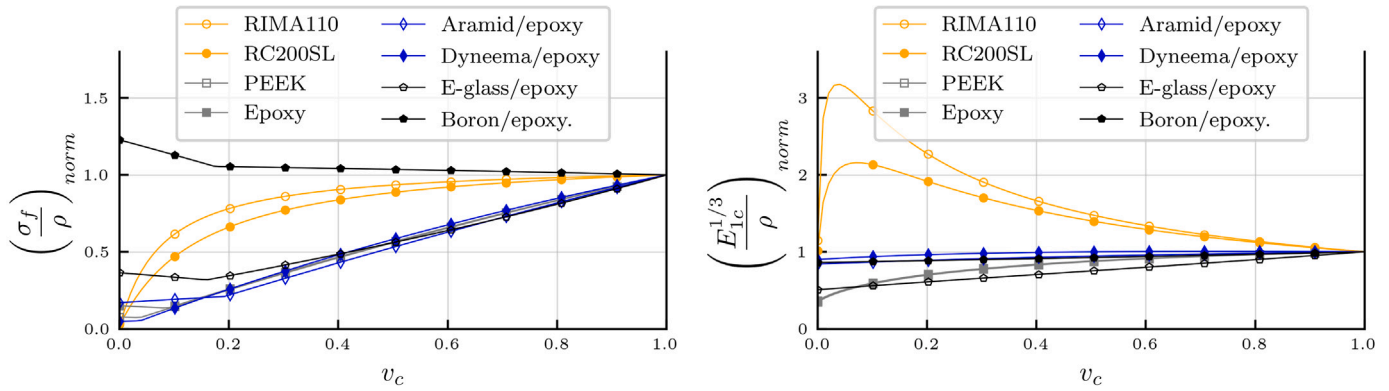- four FRP, covering a wide range of properties.

Fig. A.18. Normalised (to the values for the base CFRP material) material indexes, relevant to minimum mass design, of the hybrid load bearing layers of the proposed microstructure, as a function of the base CFRP volume content and for different choices of the hybridising material.

Table A.6

Materials and their properties considered in the evaluation of the effect of hybridisation of the load bearing layer on its specific compressive properties.

Material	ρ [g/cm³]	E_{1c} [GPa]	X_c [MPa]
RC110RIMA [63]	0.110	0.18	3.6
RC200SL [52]	0.205	0.37	9.6
PEEK [51]	1.29	3.70	118
Epoxy [51]	1.27	4.09	228
Dyneema/epoxy [64]	1.12	42	64
Aramid/epoxy [64]	1.38	64	280
E-glass/epoxy [65]	2.00	43	870
Boron/epoxy [66]	2.00	210	2930

While striving to replicate the inhomogeneity effect and the blunting mechanisms observed in nature, during our material selection process, we also prioritised retention of the specific longitudinal compressive properties of the resulting microstructure, as these are the primary selection parameters for structural applications with least weight constraints (e.g. for the aerospace sector). According to Ashby [67], material indices to maximise for structural design at minimum mass of a flat plate (with free thickness) loaded by in-plane compression are:

1. $\dfrac{\sigma_f}{\rho}$ for strength limited design (note that this is relevant to in-plane compressive failure prior to buckling, rather than post-buckling compressive failure), where σ_f is the compressive failure stress;

2. $\dfrac{E^{1/3}}{\rho}$ for stiffness limited design (buckling failure).

In a MD laminate, longitudinal compressive properties are to a large extent established by load bearing 0° plies. Hence, for selection purposes, we estimated the effect of different materials for the soft inclusions on the specific properties of the load bearing plies. Their longitudinal compressive modulus and density can be readily estimated using a simple rule of mixture (RoM) [51] as, respectively:

$$E_{1c} = E_{1c}^{CFRP} v_c + E_{1c}^{soft}(1 - v_c), \qquad (A.1)$$

$$\rho = \rho^{CFRP} v_c + \rho^{soft}(1 - v_c). \qquad (A.2)$$

where:

- E_{1c}^{CFRP}, E_{1c}^{soft}, and E_{1c}: longitudinal compressive moduli of the base CFRP material, of the soft material, and of the resulting hybrid, respectively;
- ρ^{CFRP}, ρ^{soft}, and ρ: density the base CFRP material, of the soft material, and of the resulting hybrid, respectively;
- v_c: volume fraction of the base CFRP material in the hybrid layer, with $0 < v_c < 1$.

To estimate the change to compressive strength due to hybridisation of the load bearing layers, we used the bilinear RoM, Eq. (A.3). This is commonly adopted to describe tensile strength of UD fibre-hybrid composites [68–70], but has been used by some authors also when considering compression [71,72]. While this equation is known to be generally inaccurate [69,70] (as it completely neglects any change in failure mode possibly caused by hybridisation and the possible hybrid effect [69,70]), it provides a fast tool to obtain a rough indication of the effect of the hybridising material on the compressive strength of the load bearing layers.

$$X_c = \begin{cases} X_c^{HE}(1 - v_{LE}) & \text{(valid for low } v_{LE}), \\ X_c^{LE} v_{LE} + E_{1c}^{HE} \dfrac{X_c^{LE}}{E_{1c}^{LE}}(1 - v_{LE}) & \text{(valid for high } v_{LE}). \end{cases} \qquad (A.3)$$

In Eq. (A.3), *LE* and *HE* subscripts are used to refer to the low elongation (failing at lower strain) and the high elongation (failing at higher strain) materials, respectively. A first, major, requirement on the material used for the soft inclusions is for it to have larger compressive failure strain than the base CFRP material, i.e. to behave as the *HE* material. If this is not the case, its premature failure would cause stress concentrations in the load baring CFRP strips, anticipating their failure and further reducing the overall compressive strength (beyond the reduction predicted by the bilinear RoM due to an inherent lower compressive strength of the soft material). This immediately leads to the exclusion of FRPs with low compressive strength and strain (like aramid and polymer fibre composites).

Manipulating Eqs. (A.1)–(A.3), assuming the base CFRP as the *LE* material and considering the case of high v_c (low v_c is not of interest), one can obtain an explicit expression for the specific strength of the hybrid load bearing layer containing soft inclusions:

$$\frac{X_c}{\rho} = \frac{X_c^{CFRP}}{\rho^{CFRP}}\left(1 - \frac{1 - \dfrac{E_{1c}^{soft}}{E_{1c}^{CFRP}}\dfrac{\rho^{CFRP}}{\rho^{soft}}}{1 + \dfrac{v_c}{1 - v_c}\dfrac{\rho^{CFRP}}{\rho^{soft}}}\right). \qquad (A.4)$$

In Eq. (A.4), the change in specific compressive strength of the hybrid layer, when compared to the base carbon epoxy material, is caused by the second term in parentheses. Interestingly, this term includes the specific moduli of the combined materials, rather than their specific strengths; this comes from the assumption, in Eq. (A.3) that, for high values of v_{LE}, complete failure occurs at the failure strain of the *LE* material, and that stress in the *HE* material at that strain is computed, assuming linear elastic behaviour of both hybridising materials, as $E_{1c}^{HE}\dfrac{X_c^{LE}}{E_{1c}^{LE}}$. Hence, analysing the second term in parenthesis in Eq. (A.4), we infer the following:

1. an increase in specific strength is possible if and only if the specific modulus of the soft material is higher than that of the carbon epoxy, i.e. $\frac{E_{1c}^{soft}}{\rho^{soft}} > \frac{E_{1c}^{CFRP}}{\rho^{CFRP}}$). If $\frac{E_{1c}^{soft}}{\rho^{soft}} = \frac{E_{1c}^{CFRP}}{\rho^{CFRP}}$, the specific compressive strength remains unchanged;

2. the change in specific compressive strength is inversely proportional to the term $1 + \frac{v_c}{1-v_c}\frac{\rho^{CFRP}}{\rho^{soft}}$. Neglecting the case $v_c \approx 0$, this means that changes due to differences in the specific modulus are attenuated proportionally to the term $\frac{\rho^{CFRP}}{\rho^{soft}}$. Hence, unless the specific compressive modulus can be increased, there is a strong interest in adopting a material with low density when compared to the base CFRP. On the other hand, where the specific modulus can be increased, there is an interest in materials with a higher density.

Eqs. (A.1)–(A.3) have been used to evaluate the effects on the material indices mentioned above, namely $\frac{\sigma_f}{\rho}$ and $\frac{E^{1/3}}{\rho}$, of using any of the materials listed in Table A.6 for the inclusions; the results are presented in Fig. A.18, which shows the value of the material indices, normalised to the value obtained for the base CFRP material, as a function of the hybridising material and of the base CFRP volume content, v_c. From Fig. A.18, it is evident that hybridisation with FRPs or polymers would significantly affect specific strength, the only exception being the use of a boron/epoxy composite. The use of PMI foam materials, on the other hand, would allow to retain most of the specific strength for values of v_c of interest ($v_c = 0.5$ was used in our work, see Section 3). From Fig. A.18, it also emerges that adoption of PMI foam materials can significantly improve the situation in terms of specific stiffness, which can lead to more lightweight structures for stiffness driven design situations. For these reasons, we deemed PMI foam materials as the most appropriate choice for our study and purpose, while also recognising that using other hybridising materials is of great potential interest. Finally, between the two PMI foam options presented, we chose to use RC200SL: while the difference in terms of performance with RC110RIMA is expected to be minimal, the higher strength and stiffness of RC200SL makes it much easier to use in manufacturing.

Appendix B. Supplementary data

Supplementary material related to this article can be found online at https://doi.org/10.1016/j.compositesb.2023.110867.

References

[1] Timmis AJ, Hodzic A, Koh L, Bonner M, Soutis C, Schäfer AW, et al. Environmental impact assessment of aviation emission reduction through the implementation of composite materials. Int J Life Cycle Assess 2015;20(2):233–43.

[2] Schultheisz CR, Waas AM. Compressive failure of composites, part I: Testing and micromechanical theories. Prog Aerosp Sci 1996;32(1):1–42. http://dx.doi.org/10.1016/0376-0421(94)00002-3, URL https://www.sciencedirect.com/science/article/pii/0376042194000023.

[3] Nunna S, Ravindran AR, Mroszczok J, Creighton C, Varley RJ. A review of the structural factors which control compression in carbon fibres and their composites. Compos Struct 2023;303:116293. http://dx.doi.org/10.1016/j.compstruct.2022.116293, URL https://www.sciencedirect.com/science/article/pii/S026382232201025X.

[4] Pimenta S, Gutkin R, Pinho S, Robinson P. A micromechanical model for kink-band formation: Part I — experimental study and numerical modelling. Compos Sci Technol 2009;69(7):948–55. http://dx.doi.org/10.1016/j.compscitech.2009.02.010, URL https://www.sciencedirect.com/science/article/pii/S026635380900061X.

[5] Pimenta S, Gutkin R, Pinho S, Robinson P. A micromechanical model for kink-band formation: Part II—Analytical modelling. Compos Sci Technol 2009;69(7):956–64. http://dx.doi.org/10.1016/j.compscitech.2009.02.003, URL https://www.sciencedirect.com/science/article/pii/S0266353809000529.

[6] Pinho ST, Gutkin R, Pimenta S, De Carvalho NV, Robinson P. On longitudinal compressive failure of carbon-fibre-reinforced polymer: From unidirectional to woven, and from virgin to recycled. Phil Trans R Soc A 2012;370(1965):1871–95. http://dx.doi.org/10.1098/rsta.2011.0429, arXiv:https://royalsocietypublishing.org/doi/pdf/10.1098/rsta.2011.0429.

[7] Zhang F, Zhang J, Li L, Zhu S, Shi J, Yang Y, et al. Numerical investigation on the variation of compressive failure mechanisms in unidirectional carbon fiber reinforced polymer. J Compos Mater 2021;55(11):1561–72. http://dx.doi.org/10.1177/0021998320961829, arXiv:10.1177/0021998320961829.

[8] Tsampas S, Greenhalgh E, Ankersen J, Curtis P. On compressive failure of multidirectional fibre-reinforced composites: A fractographic study. Composites A 2012;43(3):454–68. http://dx.doi.org/10.1016/j.compositesa.2011.11.013, URL https://www.sciencedirect.com/science/article/pii/S1359835X11003848.

[9] Prabhakar P, Waas AM. Micromechanical modeling to determine the compressive strength and failure mode interaction of multidirectional laminates. Composites A 2013;50:11–21. http://dx.doi.org/10.1016/j.compositesa.2013.03.006, URL https://www.sciencedirect.com/science/article/pii/S1359835X13000778.

[10] Tsampas S, Greenhalgh E, Ankersen J, Curtis P. Compressive failure of hybrid multidirectional fibre-reinforced composites. Composites A 2015;71:40–58. http://dx.doi.org/10.1016/j.compositesa.2015.01.002, URL https://www.sciencedirect.com/science/article/pii/S1359835X15000056.

[11] Bishara M, Vogler M, Rolfes R. Revealing complex aspects of compressive failure of polymer composites – part II: Failure interactions in multidirectional laminates and validation. Compos Struct 2017;169:116–28. http://dx.doi.org/10.1016/j.compstruct.2016.10.091, In Honor of Prof. Leissa URL https://www.sciencedirect.com/science/article/pii/S0263822316322322.

[12] Sun Q, Zhou G, Guo H, Meng Z, Chen Z, Liu H, et al. Failure mechanisms of cross-ply carbon fiber reinforced polymer laminates under longitudinal compression with experimental and computational analyses. Composites B 2019;167:147–60. http://dx.doi.org/10.1016/j.compositesb.2018.12.041, URL https://www.sciencedirect.com/science/article/pii/S1359836818330294.

[13] Plocher J, Mencattelli L, Narducci F, Pinho S. Learning from nature: Bio-inspiration for damage-tolerant high-performance fibre-reinforced composites. Compos Sci Technol 2021;208:108669. http://dx.doi.org/10.1016/j.compscitech.2021.108669, URL https://www.sciencedirect.com/science/article/pii/S0266353821000257.

[14] Garulli T, Greenhalgh ES, Pinho ST. A novel bio-inspired microstructure for progressive compressive failure in multidirectional composite laminates. In: Proceedings of the 20th european conference on composite materials - composites meet sustainability, Vol. 1. EPFL Lausanne, Composite Construction Laboratory; 2022, http://dx.doi.org/10.5075/epfl-298799_978-2-9701614-0-0, URL https://infoscience.epfl.ch/record/298799.

[15] Mencattelli L, Tang J, Swolfs Y, Gorbatikh L, Pinho ST. Bio-inspired design for enhanced damage tolerance of self-reinforced polypropylene/carbon fibre polypropylene hybrid composites. Composites A 2019;121:341–52. http://dx.doi.org/10.1016/j.compositesa.2019.03.028, URL https://www.sciencedirect.com/science/article/pii/S1359835X19301071.

[16] Mencattelli L, Pinho ST. Realising bio-inspired impact damage-tolerant thin-ply CFRP bouligand structures via promoting diffused sub-critical helicoidal damage. Compos Sci Technol 2019;182:107684. http://dx.doi.org/10.1016/j.compscitech.2019.107684, URL https://www.sciencedirect.com/science/article/pii/S0266353818319420.

[17] Mencattelli L, Pinho ST. Herringbone-bouligand CFRP structures: A new tailorable damage-tolerant solution for damage containment and reduced delaminations. Compos Sci Technol 2020;190:108047. http://dx.doi.org/10.1016/j.compscitech.2020.108047, URL https://www.sciencedirect.com/science/article/pii/S0266353819329203.

[18] Mencattelli L, Pinho ST. Ultra-thin-ply CFRP bouligand bio-inspired structures with enhanced load-bearing capacity, delayed catastrophic failure and high energy dissipation capability. Composites A 2020;129:105655. http://dx.doi.org/10.1016/j.compositesa.2019.105655, URL https://www.sciencedirect.com/science/article/pii/S1359835X1930404X.

[19] Ha NS, Lu G. A review of recent research on bio-inspired structures and materials for energy absorption applications. Composites B 2020;181:107496. http://dx.doi.org/10.1016/j.compositesb.2019.107496, URL https://www.sciencedirect.com/science/article/pii/S1359836819339964.

[20] Saenz-Dominguez I, Tena I, Esnaola A, Sarrionandia M, Torre J, Aurrekoetxea J. Design and characterisation of cellular composite structures for automotive crash-boxes manufactured by out of die ultraviolet cured pultrusion. Composites B 2019;160:217–24. http://dx.doi.org/10.1016/j.compositesb.2018.10.046, URL https://www.sciencedirect.com/science/article/pii/S1359836818306899.

[21] Pehlivan L, Baykasoğlu C. An experimental study on the compressive response of CFRP honeycombs with various cell configurations. Composites B 2019;162:653–61. http://dx.doi.org/10.1016/j.compositesb.2019.01.044, URL https://www.sciencedirect.com/science/article/pii/S1359836818331810.

[22] Ghazlan A, Ngo T, Tan P, Xie YM, Tran P, Donough M. Inspiration from nature's body armours – a review of biological and bioinspired composites. Composites B 2021;205:108513. http://dx.doi.org/10.1016/j.compositesb.2020.108513, URL https://www.sciencedirect.com/science/article/pii/S1359836820335605.

[23] Häsä R, Pinho S. A novel aluminium/CFRP hybrid composite with a bio-inspired crossed-lamellar microstructure for preservation of structural integrity. Compos Sci Technol 2019;182:107760. http://dx.doi.org/10.1016/j.compscitech.2019.107760, URL https://www.sciencedirect.com/science/article/pii/S0266353818331075.

[24] Häsä R, Pinho S. A three-level hybrid metal/in-plane-CFRP/crossed-lamellar microstructure concept for containment applications. Composites A 2019;126:105609. http://dx.doi.org/10.1016/j.compositesa.2019.105609, URL https://www.sciencedirect.com/science/article/pii/S1359835X19303586.

[25] Narducci F, Pinho S. Exploiting nacre-inspired crack deflection mechanisms in CFRP via micro-structural design. Compos Sci Technol 2017;153:178–89. http://dx.doi.org/10.1016/j.compscitech.2017.08.023, URL https://www.sciencedirect.com/science/article/pii/S0266353817300167.

[26] Narducci F, Lee K-Y, Pinho S. Interface micro-texturing for interlaminar toughness tailoring: A film-casting technique. Compos Sci Technol 2018;156:203–14. http://dx.doi.org/10.1016/j.compscitech.2017.10.016, URL https://www.sciencedirect.com/science/article/pii/S0266353817316342.

[27] Narducci F, Lee K-Y, Pinho S. Realising damage-tolerant nacre-inspired CFRP. J Mech Phys Solids 2018;116:391–402. http://dx.doi.org/10.1016/j.jmps.2018.04.004, URL https://www.sciencedirect.com/science/article/pii/S0022509618300851.

[28] Narducci F, Pinho S. Interaction between nacre-like CFRP mesolayers and long-fibre interlayers. Compos Struct 2018;200:921–8. http://dx.doi.org/10.1016/j.compstruct.2018.05.103, URL https://www.sciencedirect.com/science/article/pii/S0263822318311887.

[29] Bullegas G, Pinho ST, Pimenta S. Engineering the translaminar fracture behaviour of thin-ply composites. Compos Sci Technol 2016;131:110–22. http://dx.doi.org/10.1016/j.compscitech.2016.06.002, URL https://www.sciencedirect.com/science/article/pii/S0266353816304468.

[30] Bullegas G, Benoliel J, Fenelli PL, Pinho ST, Pimenta S. Towards quasi isotropic laminates with engineered fracture behaviour for industrial applications. Compos Sci Technol 2018;165:290–306. http://dx.doi.org/10.1016/j.compscitech.2018.07.004, URL https://www.sciencedirect.com/science/article/pii/S0266353818305840.

[31] Tang J, Swolfs Y, Aslani A, Mencattelli L, Bullegas G, Pinho ST, et al. Engineering tensile behavior of hybrid carbon fiber/self-reinforced polypropylene composites by bio-inspired fiber discontinuities. Composites B 2019;178:107502. http://dx.doi.org/10.1016/j.compositesb.2019.107502, URL https://www.sciencedirect.com/science/article/pii/S1359836819324813.

[32] Aizenberg J, Weaver JC, Thanawala MS, Sundar VC, Morse DE, Fratzl P. Skeleton of Euplectella sp.: Structural hierarchy from the nanoscale to the macroscale. Science 2005;309(5732):275–8. http://dx.doi.org/10.1126/science.1112255, arXiv:https://www.science.org/doi/pdf/10.1126/science.1112255.

[33] Weaver JC, Milliron GW, Allen P, Miserez A, Rawal A, Garay J, et al. Unifying design strategies in demosponge and hexactinellid skeletal systems. J Adhes 2010;86(1):72–95. http://dx.doi.org/10.1080/00218460903417917, arXiv:10.1080/00218460903417917.

[34] Levi C, Barton J, Guillemet C, Le Bras E, Lehuede P. A remarkably strong natural glassy rod: The anchoring spicule of the monorhaphis sponge. J Mater Sci Lett 1989;8(3):337–9.

[35] Müller W, Wang X, Kropf K, Ushijima H, Geurtsen W, Eckert C, et al. Bioorganic/inorganic hybrid composition of sponge spicules: Matrix of the giant spicules and of the comitalia of the deep sea hexactinellid monorhaphis. J Struct Biol 2008;161:188–203. http://dx.doi.org/10.1016/j.jsb.2007.10.009.

[36] Miserez A, Weaver JC, Thurner PJ, Aizenberg J, Dauphin Y, Fratzl P, et al. Effects of laminate architecture on fracture resistance of sponge biosilica: Lessons from nature. Adv Funct Mater 2008;18(8):1241–8. http://dx.doi.org/10.1002/adfm.200701135.

[37] Kolednik O, Predan J, Fischer FD, Fratzl P. Bioinspired design criteria for damage-resistant materials with periodically varying microstructure. Adv Funct Mater 2011;21(19):3634–41. http://dx.doi.org/10.1002/adfm.201100443.

[38] Kolednik O, Predan J, Fischer F, Fratzl P. Improvements of strength and fracture resistance by spatial material property variations. Acta Mater 2014;68:279–94. http://dx.doi.org/10.1016/j.actamat.2014.01.034, URL https://www.sciencedirect.com/science/article/pii/S1359645414000512.

[39] Wagner HD. Hierarchical interfaces as fracture propagation traps in natural layered composites. Materials 2021;14(22):6855. http://dx.doi.org/10.3390/ma14226855.

[40] Kolednik O, Kasberger R, Sistaninia M, Predan J, Kegl M. Development of damage-tolerant and fracture-resistant materials by utilizing the material inhomogeneity effect. J Appl Mech 2019;86(11). http://dx.doi.org/10.1115/1.4043829, 111004 arXiv:https://asmedigitalcollection.asme.org/appliedmechanics/article-pdf/86/11/111004/5433484/jam_86_11_111004.pdf.

[41] Tiwari A, Wiener J, Arbeiter F, Pinter G, Kolednik O. Application of the material inhomogeneity effect for the improvement of fracture toughness of a brittle polymer. Eng Fract Mech 2020;224:106776. http://dx.doi.org/10.1016/j.engfracmech.2019.106776, URL https://www.sciencedirect.com/science/article/pii/S0013794419309312.

[42] Waly C, Petersmann S, Arbeiter F. Multimaterial extrusion-based additive manufacturing of compliant crack arrester: Influence of interlayer length, thickness, and applied strain rate. Adv Energy Mater 2021;n/a(n/a):2101703. http://dx.doi.org/10.1002/adem.202101703, URL https://onlinelibrary.wiley.com/doi/abs/10.1002/adem.202101703.

[43] Wiener J, Kaineder H, Kolednik O, Arbeiter F. Optimization of mechanical properties and damage tolerance in polymer-mineral multilayer composites. Materials 2021;14(4):725. http://dx.doi.org/10.3390/ma14040725, URL http://dx.doi.org/10.3390/ma14040725.

[44] Wiener J, Arbeiter F, Kolednik O, Pinter G. Influence of layer architecture on fracture toughness and specimen stiffness in polymer multilayer composites. Mater Des 2022;219:110828. http://dx.doi.org/10.1016/j.matdes.2022.110828, URL https://www.sciencedirect.com/science/article/pii/S0264127522004506.

[45] Arteiro A, Furtado C, Catalanotti G, Linde P, Camanho P. Thin-ply polymer composite materials: A review. Composites A 2020;132:105777. http://dx.doi.org/10.1016/j.compositesa.2020.105777, URL https://www.sciencedirect.com/science/article/pii/S1359835X20300154.

[46] Fleck N. Compressive failure of fiber composites. In: Hutchinson JW, Wu TY, editors. In: Advances in applied mechanics, vol. 33, Elsevier; 1997, p. 43–117. http://dx.doi.org/10.1016/S0065-2156(08)70385-5, URL https://www.sciencedirect.com/science/article/pii/S0065215608703855.

[47] Gutkin R, Pinho S, Robinson P, Curtis P. On the transition from shear-driven fibre compressive failure to fibre kinking in notched CFRP laminates under longitudinal compression. Compos Sci Technol 2010;70(8):1223–31. http://dx.doi.org/10.1016/j.compscitech.2010.03.010, URL https://www.sciencedirect.com/science/article/pii/S0266353810001119.

[48] PYROFIL™ MR70 data sheet. 2022, https://northerncomposites.com/wp-content/uploads/2020/07/MR-70-12P20140204.pdf [Accessed last: 29 Nov 2022].

[49] NTPT THINPREG™ 402 data sheet. 2022, https://www.thinplytechnology.com/assets/mesimages/NTPT-DS-ThinPreg-402-May2017-v3.pdf [Accessed last: 31 Oct 2022].

[50] Meng M, Le H, Rizvi M, Grove S. The effects of unequal compressive/tensile moduli of composites. Compos Struct 2015;126:207–15. http://dx.doi.org/10.1016/j.compstruct.2015.02.064, URL https://www.sciencedirect.com/science/article/pii/S026382231500152X.

[51] Barbero EJ. Introduction to composite materials design. CRC Press; 2017.

[52] Product information ROHACELL© SL. 2022, https://products.evonik.com/assets/33/98/243398.pdf [Accessed last: 04 Oct 2022].

[53] Fratzl P, Gupta HS, Fischer FD, Kolednik O. Hindered crack propagation in materials with periodically varying Young's modulus—Lessons from biological materials. Adv Mater 2007;19(18):2657–61. http://dx.doi.org/10.1002/adma.200602394, arXiv:https://onlinelibrary.wiley.com/doi/pdf/10.1002/adma.200602394.

[54] Amacher R, Cugnoni J, Botsis J, Sorensen L, Smith W, Dransfeld C. Thin ply composites: Experimental characterization and modeling of size-effects. Compos Sci Technol 2014;101:121–32. http://dx.doi.org/10.1016/j.compscitech.2014.06.027, URL https://www.sciencedirect.com/science/article/pii/S0266353814002280.

[55] Wang Y, Chai Y, Soutis C, Withers PJ. Evolution of kink bands in a notched unidirectional carbon fibre-epoxy composite under four-point bending. Compos Sci Technol 2019;172:143–52. http://dx.doi.org/10.1016/j.compscitech.2019.01.014, URL https://www.sciencedirect.com/science/article/pii/S0266353818310418.

[56] Pinho S, Darvizeh R, Robinson P, Schuecker C, Camanho P. Material and structural response of polymer-matrix fibre-reinforced composites. J Compos Mater 2012;46(19–20):2313–41. http://dx.doi.org/10.1177/0021998312454478, arXiv:10.1177/0021998312454478.

[57] Camanho PP, Dávila CG, Pinho ST, Iannucci L, Robinson P. Prediction of in situ strengths and matrix cracking in composites under transverse tension and in-plane shear. Composites A 2006;37(2):165–76. http://dx.doi.org/10.1016/j.compositesa.2005.04.023, CompTest 2004 URL https://www.sciencedirect.com/science/article/pii/S1359835X05002526.

[58] Catalanotti G, Camanho P, Marques A. Three-dimensional failure criteria for fiber-reinforced laminates. Compos Struct 2013;95:63–79. http://dx.doi.org/10.1016/j.compstruct.2012.07.016, URL https://www.sciencedirect.com/science/article/pii/S0263822312003443.

[59] LePage WS, Daly SH, Shaw JA. Cross polarization for improved digital image correlation. Exp Mech 2016;56(6):969–85.

[60] ABAQUS/standard user's manual, version 2021. Dassault Systèmes Simulia Corp.

[61] Squires CA, Netting KH, Chambers AR. Understanding the factors affecting the compressive testing of unidirectional carbon fibre composites. Composites B 2007;38(4):481–7. http://dx.doi.org/10.1016/j.compositesb.2006.08.002, URL https://www.sciencedirect.com/science/article/pii/S1359836806001168.

[62] Pinho S, Robinson P, Iannucci L. Fracture toughness of the tensile and compressive fibre failure modes in laminated composites. Compos Sci Technol 2006;66(13):2069–79. http://dx.doi.org/10.1016/j.compscitech.2005.12.023, URL https://www.sciencedirect.com/science/article/pii/S026635380600011X.

[63] Product information ROHACELL© RIMA. 2022, https://products.evonik.com/assets/32/67/243267.pdf [Accessed last: 04 Oct 2022].

[64] van Dingenen J. High performance dyneema fibres in composites. Mater Des 1989;10(2):101–4. http://dx.doi.org/10.1016/S0261-3069(89)80021-4, URL https://www.sciencedirect.com/science/article/pii/S0261306989800214.

[65] Carlsson LA, Adams DF, Pipes RB. Experimental characterization of advanced composite materials. CRC Press; 2014.

[66] Specialty materials website - boron fiber products. 2022, https://www.specmaterials.com/services-4 [Accessed last: 07 Oct 2022].

[67] Ashby MF, editor. Appendix c - material indices. In: Materials selection in mechanical design (fourth edition). 4th Ed.. Oxford: Butterworth-Heinemann; 2011, p. 559–64. http://dx.doi.org/10.1016/B978-1-85617-663-7.00020-5, URL https://www.sciencedirect.com/science/article/pii/B9781856176637000205.

[68] Aveston J, Kelly A. Tensile first cracking strain and strength of hybrid composites and laminates. Phil Trans R Soc A 1980;294(1411):519–34, Cited by: 62 URL https://www.scopus.com/inward/record.uri?eid=2-s2.0-1642589642&partnerID=40&md5=1e0de26f868ac2e653115462ad7b3b9d.

[69] Swolfs Y, Gorbatikh L, Verpoest I. Fibre hybridisation in polymer composites: A review. Composites A 2014;67:181–200. http://dx.doi.org/10.1016/j.compositesa.2014.08.027.

[70] Swolfs Y, Verpoest I, Gorbatikh L. Recent advances in fibre-hybrid composites: Materials selection, opportunities and applications. Int Mater Rev 2019;64(4):181–215. http://dx.doi.org/10.1080/09506608.2018.1467365.

[71] Wang Q, Wu W, Li W. Compression properties of interlayer and intralayer carbon/glass hybrid composites. Polymers 2018;10(4). http://dx.doi.org/10.3390/polym10040343, URL https://www.mdpi.com/2073-4360/10/4/343.

[72] Rajpurohit A, Joannès S, Singery V, Sanial P, Laiarinandrasana L. Hybrid effect in in-plane loading of carbon/glass fibre based inter- and intraply hybrid composites. J Compos Sci 2020;4(1). http://dx.doi.org/10.3390/jcs4010006, URL https://www.mdpi.com/2504-477X/4/1/6.